Laterally heterogeneous scattering explains Lg blockage in the Pyrenees

C. Sens-Schönfelder,[1] L. Margerin,[2] and M. Campillo[3]

[1]   We present an algorithm to simulate the propagation of seismic energy in a model that contains both deterministic structure and statistically described small-scale heterogeneities. With this algorithm, we study the propagation of seismic waves through the Pyrenees. Using a series of seismograms, the variations of the attenuation properties of the crust along the Pyrenean axis are illustrated. The western Pyrenees exhibit strong attenuation of crustal phases, a phenomenon known as Lg blockage. Previous studies demonstrated that the large-scale velocity structure of the western Pyrenees cannot explain the strong lateral variations of attenuation along the Pyrenean range. In this paper we present a model that is able to explain the principal observations. We propose that the Lg blockage is caused by a perturbed region of the crust with scattering and anelastic properties that differ markedly from the surrounding crust. Numerical simulations of the elastic radiative transfer equation in a layered medium show that it is possible to model the observed Lg blockage with increased scattering in the perturbed body. In order to explore the relative importance of scattering and attenuation we performed an inversion of the data using a genetic algorithm. Our study reveals that stronger intrinsic attenuation in the perturbed body improves the fit to the data but that intrinsic attenuation alone cannot explain the observations. Our work puts forward the role of multiple scattering in the attenuation mechanism of crustal phases.

1.   Introduction

[2]   Investigations of the heterogeneity in the Earth's crust based on coda analysis began with *Aki and Chouet* [1975], who suggested that the seismic coda is due to scattering of elastic waves at randomly distributed small-scale heterogeneity. Since then various approaches have been suggested to model the scattering process and to infer information about the subsurface from the scattered waves. Most common approaches make use of the theory of radiative transfer in one of the numerous approximations. We begin section 2 with a short discussion of the limitations of the currently available approximations of the radiative transfer equation before we present an algorithm that solves the energy transfer problem with nonisotropic scattering in a three dimensional structure with laterally variable heterogeneity.

[3]   In sections 3 and 4 we discuss the tectonic setting of the Pyrenees and the observation of disturbed propagation of Lg waves through the western part of this mountain range. This phenomenon, termed Lg blockage because of the almost perfect extinction cannot be explained by the large-scale velocity structure. We present a model in section 5 and 6 that allows to explain the properties of the Lg propagation through the Pyrenees with laterally heterogeneous scattering. The results are discussed in section 7.

[4]   The reader interested in the analysis of Lg blockage may want to jump directly to the application in the Pyrenees (section 3) and leave the technical aspects of section 2 for a second reading.

2.   Monte Carlo Simulations of Elastic Wave Energy in the Presence of Deterministic Structure

2.1.   Radiative Transfer Theory in Seismology

[5]   Many applications of radiative transfer theory are based on the approximation of acoustic and isotropic scattering [*Hoshiba et al.*, 1991; *Fehler et al.*, 1992; *Hoshiba*, 1993]. For the analysis of the S wave coda and the estimation of basic medium and source/site parameters this approximation is useful [*Sens-Schönfelder and Wegler*, 2006]. The main shortcoming for practical applications is the inability of this approximation to model the P wave and its coda. From the theoretical point of view, the limitation to acoustic and isotropic scattering implies a severe simplification of the physics of wave propagation through a heterogeneous elastic medium. Here, an algorithm is introduced that solves the radiative transfer equation with less restrictive approximations. The fundamental improvement

---

[1]Institute of Geophysics and Geology, University of Leipzig, Leipzig, Germany.
[2]Centre Européen de Recherche et d'Enseignement des Géosciences de l'Environnement, Aix en Provence, France.
[3]Laboratoire de Géophysique Interne et Tectonophysique, Université Joseph Fourier, Grenoble, France.

is the simulation of elastic energy propagation with conversion between P and S modes in a three-dimensional model that contains deterministic structure like velocity gradients and discontinuities.

[6] The radiative transfer of elastic energy in a model with deterministic velocity structure is perhaps the most accurate approach to the description of the scattering of seismic waves in Earth's crust at our disposal. Numerous approximation to this situation can be found in the literature. The simplest approaches assume isotropic single scattering of acoustic energy in an infinite medium [e.g., *Aki and Chouet*, 1975]. Isotropic means that there is no preferred direction of scattering. The acoustic approximation limits the scattering to depolarized S waves. P waves and mode conversions are neglected. The single scattering approach assumes that waves are scattered only once on their way from the source to the receiver. Since there is strong evidence for multiple scattering of seismic waves in the crust [*Hennino et al.*, 2001; *Larose et al.*, 2004], this approximation strongly limits the applicability of this approach. The diffusion approximation [*Aki and Chouet*, 1975; *Dainty and Toksöz*, 1981; *Wegler and Lühr*, 2001] that assumes strong scattering is the other extreme and is only applicable for late lapse times of crustal seismic records. Multiple scattering is suitable for the intermediate range of moderate scattering [e.g., *Hoshiba*, 1991].

[7] The approximation of isotropic scattering was replaced by nonisotropic scattering by *Hoshiba* [1995]. The modeling of seismogram envelopes using elastic scattering at distributed spheres is from *Margerin et al.* [2000]. This was extended to continuous random inhomogeneities by *Shearer and Earle* [2004] and *Przybilla et al.* [2006]. The superposition of isotropic scatterers on a simple depth-dependent velocity structure was first modeled by *Hoshiba* [1997] and by *Margerin et al.* [1998] for acoustic waves. In this work, all these ingredients are brought together, and an algorithm is presented that is able to synthesize seismogram envelopes for multiple nonisotropic scattering of elastic waves at randomly distributed heterogeneities in deterministic macroscopic structure.

2.2. Elastic Radiative Transfer Theory

[8] The central quantity of transfer theory is the radiance or specific intensity $I(\mathbf{n}, \mathbf{r})$. It measures the energy flux from a radiating surface into a unit solid angle around direction $\mathbf{n}$. This angular spectrum of the energy flux may be a local quantity and depends on position $\mathbf{r}$. An equivalent representation of the energy flux is provided by the local, angularly-resolved, energy density $a(\mathbf{n}, \mathbf{x})$ that is related to the radiance by

$$a(\mathbf{n}, \mathbf{x}) = \frac{1}{v} I(\mathbf{n}, \mathbf{x}), \qquad (1)$$

where v is the wave velocity. In equation (1) and in what follows, we adopt the convention that the radiance and related quantities implicitly depend on time and frequency. This choice is physically sound since, on one hand, the energy transport in seismology is always nonstationary while, on the other hand, the propagation medium is static which ensures that frequency is conserved along a ray.

[9] In the classical book by *Chandrasekhar* [1960], the radiative transfer equation that describes the radiance is
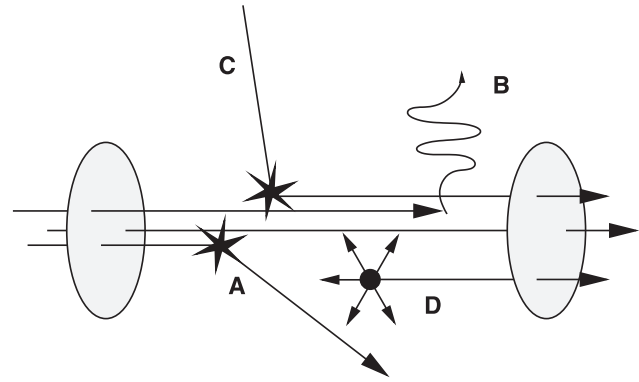

Figure 1. Illustration of the energy conservation in the energy transfer equation. The flux in direction $\mathbf{n}$ is diminished by scattering into other directions (A) and by dissipation (B). A gain of the flux results from scattering from other directions into direction $\mathbf{n}$ (C) and from sources (D).

introduced phenomenologically to describe light propagation through atmospheres. The phenomenological view of the transport problem is based on considerations of conservation of energy flux in direction $\mathbf{n}$ at a fixed point in space as illustrated in Figure 1. The flux in direction $\mathbf{n}$ is diminished by scattering into other directions (A) and by dissipation (B). It is increased by scattering from other directions into direction $\mathbf{n}$ (C) and by sources (D).

[10] These heuristic considerations are physically transparent and seem intuitively convincing without further explanations. For several decades this field developed without complete physical foundations and independently of wave physics. A rigorous statistical substantiation of this concept was achieved when the direct connection between the angular Fourier transform of the radiance and the spatial coherence function of the wavefield was discovered. The coherence function of a monochromatic wavefield $u(\mathbf{x}, t) = A(\mathbf{x})e^{i(k\mathbf{nx}-\omega t)}$ is defined as (omitting the time dependence)

$$\Gamma(\mathbf{x}, \rho) = \langle u(\mathbf{x} + \rho)u^*(\mathbf{x})\rangle. \qquad (2)$$

It is given by the angular Fourier transform of the radiance [*Apresyan and Kravtsov*, 1996, p. 22]:

$$\Gamma(\mathbf{x}, \rho) \propto \int I(\mathbf{n}, \mathbf{x})e^{ik\mathbf{n}\rho}d\Omega_{\mathbf{n}}. \qquad (3)$$

Equation (3) indicates that the radiance can be interpreted as the angular spectrum of the wavefield. In the case of elastic waves, the connection between radiative transfer and the underlying wave equation has been established by *Ryzhik et al.* [1996] and *Weaver* [1990]. The elastic transport equation takes the form of a system of two coupled integrodifferential equations for the P wave intensity and the 2×2 coherence matrix for the S waves. The coherence matrix $\hat{I}$ takes into account the two S polarizations with degenerate dispersion laws together with their phase relation. It is defined as [*Apresyan and Kravtsov*, 1996, p. 72]

$$\hat{I} = \begin{bmatrix} I_{\theta\theta} & I_{\theta\phi} \\ I_{\phi\theta} & I_{\phi\phi} \end{bmatrix} = c\begin{bmatrix} \langle A_\theta A_\theta^* \rangle & \langle A_\theta A_\phi^* \rangle \\ \langle A_\phi A_\theta^* \rangle & \langle A_\phi A_\phi^* \rangle \end{bmatrix}, \qquad (4)$$
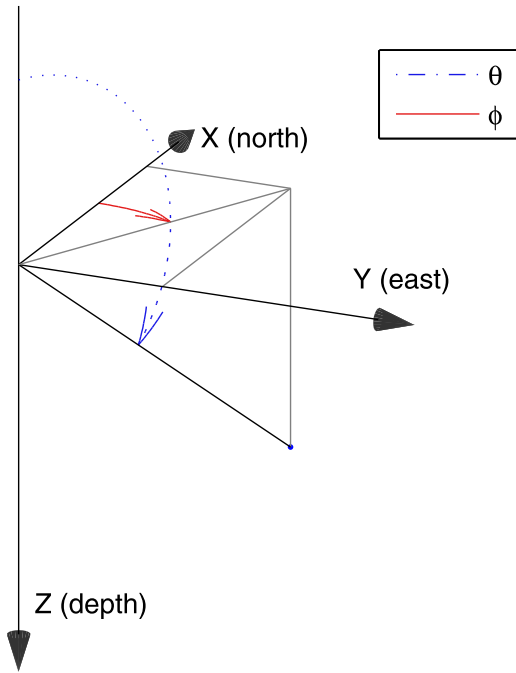
Figure 2. Illustration of the relations between the geographical, the Cartesian, and the polar coordinate systems as they are used in the algorithm. Angles are identified by color.

where the subscripts θ and ϕ refer to unit vectors in the directions of increasing angles θ and ϕ of the polar coordinate system shown in Figure 2. A_θ and A_ϕ represent the complex amplitudes of a plane S wave propagating in direction (θ, ϕ), and c is a proportionality coefficient related to the local elastic properties. Alternatively, the polarization can be described by a Stokes vector. Following *Turner and Weaver* [1994] and *Margerin et al.* [2000], we define a Stokes vector that includes the P wave intensity I^P as

$$P = \begin{pmatrix} I^P \\ I^S_\theta \\ I^S_\phi \\ U \\ V \end{pmatrix} = \begin{pmatrix} I^P \\ I_{\theta\theta} \\ I_{\phi\phi} \\ I_{\phi\theta} + I_{\theta\phi} \\ i(I_{\phi\theta} - I_{\theta\phi}) \end{pmatrix} = \mathbf{c} \begin{pmatrix} \langle |A^P|^2 \rangle \\ \langle |A_\theta|^2 \rangle \\ \langle |A_\phi|^2 \rangle \\ 2\mathrm{Re}\langle A_\theta A^*_\phi \rangle \\ 2\mathrm{Im}\langle A_\theta A^*_\phi \rangle \end{pmatrix}, \quad (5)$$

where $\mathbf{c}$ is a diagonal matrix of proportionality constants with elements $c_1 = \rho\omega^2\alpha/2$ and $c_{2\ldots5} = \rho\omega^2\beta/2$. I^S_θ and I^S_ϕ correspond to the intensities of SV and SH waves, respectively. The parameters U and V can be written in terms of the phase difference δ between the S wave motions measured along the θ and ϕ directions:

$$U = 2c_4 \langle A_\theta A_\phi \cos(\delta) \rangle \quad (6)$$

$$V = 2c_5 \langle A_\theta A_\phi \sin(\delta) \rangle. \quad (7)$$

[11] The Stokes vector provides a full description of the state of polarization including fully (i.e., linear and elliptical) or partially polarized waves. The character of a seismic shear source and the structure of the scattering coefficients (Appendix D) allows us to simplify the treatment of polar-

izations. A point shear dislocation emits completely linearly polarized waves for which the phase shift δ is zero. In addition, we note that for sufficiently weak scatterers, the two S components remain in phase upon scattering. Neglecting the phases shifts that may occur at postcritical reflections, we can simplify the treatment of the polarization by assuming that S waves are always linearly polarized. Since no elliptical polarization occurs, we can omit the V component of the Stokes vector which is zero for linear polarized waves (compare equation (7) for $\delta = 0$). The U component is determined by the following relation that holds for completely polarized waves [*Apresyan and Kravtsov*, 1996, p. 74]:

$$\left(I^S_\theta + I^S_\phi\right)^2 = \left(I^S_\theta - I^S_\phi\right)^2 + U^2 + V^2. \quad (8)$$

For $V = 0$, U is defined by I^S_θ and I^S_ϕ. The approximation of linear polarization allows us to write the transport equations as system of three coupled scalar equations for I^P, I^S_θ and I^S_ϕ. The equations follow directly from a local energy balance in a multimode system as described by *Apresyan and Kravtsov* [1996, p. 84]. The transport equation for I^P reads

$$\left(\frac{\partial}{\alpha_0\partial t} + \mathbf{n} \cdot \nabla\right) I^P(\mathbf{n}, \mathbf{r}) = -\left(g^{PP}_0 + g^{PS}_0 + \frac{\omega}{\alpha^I_0 Q^P}\right) I^P(\mathbf{n}, \mathbf{r})$$
$$+ \int_{4\pi} g^{PP}(\Theta) I^P(\mathbf{n}', \mathbf{r}) d\Omega_{n'}$$
$$+ \int_{4\pi} g^{SP}(\Theta, \Phi_\theta) I^S_\theta(\mathbf{n}', \mathbf{r}) d\Omega_{n'}$$
$$+ \int_{4\pi} g^{SP}(\Theta, \Phi_\phi) I^S_\phi(\mathbf{n}', \mathbf{r}) d\Omega_{n'}. \quad (9)$$

In equation (9), we used the following notation: α_0 is the mean P wave velocity, g^{AB}_0 denotes the total scattering coefficient defined in equation (D23), and $^I Q^P$ is the intrinsic quality factor of P waves introduced in Appendix E. The scattering coefficients $g^{AB}(\Theta, \Phi)$ are discussed in detail in Appendix D. These coefficients are assumed to be given in the local scattering coordinate system. Θ is the scattering angle between the incoming and outgoing directions $\mathbf{n}$ and $\mathbf{n}'$, and Φ is the angle between the polarization direction of the incident wave and the scattering plane spanned by $\mathbf{n}$ and $\mathbf{n}'$. Note that Φ refers to a different angle in the integrals involving I^S_ϕ and I^S_θ. Finally, the differential solid angle is defined by $d\Omega_{n'} = \sin(\Theta) d\Theta d\Phi$. Using similar notations, the transport equations for I^S_θ and I^S_ϕ read

$$\left(\frac{\partial}{\beta_0\partial t} + \mathbf{n} \cdot \nabla\right) I^S_\theta(\mathbf{n}, \mathbf{r}) = -\left(g^{SS}_0 + g^{SP}_0 + \frac{\omega}{\beta^I_0 Q^S}\right) I^S_\theta(\mathbf{n}, \mathbf{r})$$
$$+ \int_{4\pi} g^{SS}_l(\Theta, \Phi_\theta) I^S_\theta(\mathbf{n}', \mathbf{r}) \cos^2(\psi) d\Omega_{n'}$$
$$+ \int_{4\pi} g^{SS}_r(\Theta, \Phi_\theta) I^S_\theta(\mathbf{n}', \mathbf{r}) \sin^2(\psi) d\Omega_{n'}$$
$$+ \int_{4\pi} g^{SS}_l(\Theta, \Phi_\phi) I^S_\phi(\mathbf{n}', \mathbf{r}) \cos^2(\psi) d\Omega_{n'}$$
$$+ \int_{4\pi} g^{SS}_r(\Theta, \Phi_\phi) I^S_\phi(\mathbf{n}', \mathbf{r}) \sin^2(\psi) d\Omega_{n'}$$
$$+ \int_{4\pi} g^{PS}(\Theta) I^P(\mathbf{n}', \mathbf{r}) \cos^2(\psi) d\Omega_{n'}, \quad (10)$$
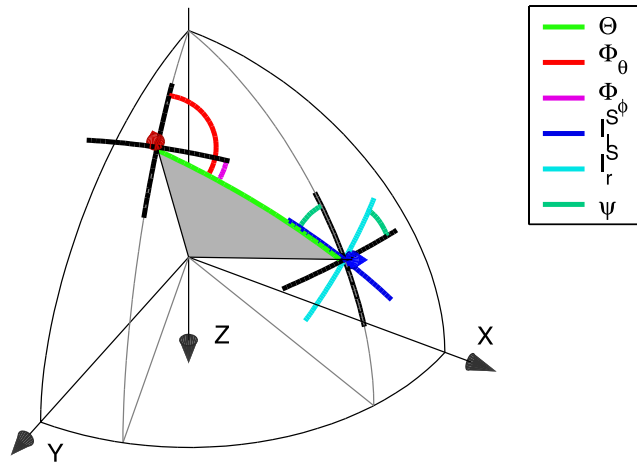
Figure 3. Illustration of the S polarization directions in the radiative transfer equations. Angles are identified by color of the arcs. The red and blue arrows indicate directions n' and n, respectively. The blue lines labeled I_l^S and I_r^S indicate the directions of polarization of the parallel and perpendicular intensity components, respectively.

and

$$\left(\frac{\partial}{\beta_0\partial t}+\mathbf{n}\cdot\nabla\right)I_\phi^S(\mathbf{n},\mathbf{r}) = -\left(g_0^{SS}+g_0^{SP}+\frac{\omega}{\beta_0^l Q^S}\right)I_\phi^S(\mathbf{n},\mathbf{r})$$

$$+\int_{4\pi}g_l^{SS}(\Theta,\Phi_\theta)I_\theta^S(\mathbf{n}',\mathbf{r})\sin^2(\psi)d\Omega_{n'}$$

$$+\int_{4\pi}g_r^{SS}(\Theta,\Phi_\theta)I_\theta^S(\mathbf{n}',\mathbf{r})\cos^2(\psi)d\Omega_{n'}$$

$$+\int_{4\pi}g_l^{SS}(\Theta,\Phi_\phi)I_\phi^S(\mathbf{n}',\mathbf{r})\sin^2(\psi)d\Omega_{n'}$$

$$+\int_{4\pi}g_r^{SS}(\Theta,\Phi_\phi)I_\phi^S(\mathbf{n}',\mathbf{r})\cos^2(\psi)d\Omega_{n'}$$

$$+\int_{4\pi}g^{PS}(\Theta)I^P(\mathbf{n}',\mathbf{r})\sin^2(\psi)d\Omega_{n'},$$

(11)

respectively. The angle ψ denotes the dihedral angle between the scattering plane and the vertical plane that contains the vector $\mathbf{n}$. This form of the transfer equations is unusual but it best refers to the way we solve the equations with the Monte Carlo technique. It is worth mentioning that two rotations of the Stokes vector are somewhat hidden in equations (10) and (11). The first corresponds to the rotation of the scattering coefficients in a local frame with orientation of the polar axis along $\mathbf{n}'$ and Φ measured from the direction of polarization. This results in the use of the two angles Φ_θ and Φ_ϕ for the two polarizations which of course obey the relation $\Phi_\theta = \pi/2 + \Phi_\phi$. The geometry is depicted in Figure 3. The second rotation is encapsulated in the $\sin^2(\psi)$ and $\cos^2(\psi)$ terms and projects the intensities $I_r^S(\mathbf{n})$ and $I_l^S(\mathbf{n})$ measured in the directions perpendicular and parallel to the scattering plane onto the θ and ϕ directions, respectively. The $\sin^2(\psi)$ and $\cos^2(\psi)$ terms correspond to the rotation matrix for the Stokes vector [*Ishimaru*, 1978]. When applied to the scattering matrix defined in a local frame, the two rotations yield the Müller matrix. Because the scattering coefficients are evaluated in the local frame in the Monte Carlo simulations, we do not discuss this matrix further and refer the interested reader to *Margerin et al.* [2000].

2.3. Monte Carlo Techniques to Solve the Radiative Transfer Equation

[12] Monte Carlo techniques are widely used to solve transport problems. Applications range from light propagation through atmospheres, and neutron scattering to global illumination computations in computer graphics. In seismology there are two different strategies to solve the transfer equation with Monte Carlo methods. The first method that one could refer to as "probability summation method" was first used by *Hoshiba* [1991]. The idea of this approach is to simulate the propagation of particles through the medium and evaluate the probability that a particle is scattered toward a receiver at every scattering event. This probability which depends on the scattering coefficient (Appendix D2), the geometry of the incident ray, and the direction to the receiver, is multiplied by a factor that accounts for attenuation and geometrical spreading. The resulting quantity is the contribution to the energy density at the site of the receiver at the potential arrival time of the particle. So each scattering event contributes to the energy density estimate at the receiver. This method allows to measure the energy density at point-like receivers which is useful if there is weak symmetry in the model.

[13] The second method for Monte Carlo simulations in seismology was first used by *Gusev and Abubakirov* [1987] and could be called "particle counting method." Here the particles are also propagated through the medium but do only contribute to the energy density estimate at the receiver if they pass through a finite size volume placed around the receiver. This is very efficient if there is some symmetry in the model that allows the use of, e.g., a spherical shell as receiver volume. When symmetry is weak, which inevitably occurs if realistic shear sources are simulated, the efficiency decreases drastically because many particles that never pass through the small receiver volume delay the simulation.

[14] The principle source of the fluctuations in the energy density estimates is the randomness of the particles' trajectories. In the probability summation method the probability of the particle to be scattered toward the receiver and the geometrical spreading between the scattering point and the receiver are additional sources of fluctuations. For strongly anisotropic scattering these fluctuations increase dramatically and appear to be non-Gaussian. The envelopes have a relatively smooth lower level but irregular spikes which strongly exceed this surrounding level. For increasingly larger numbers of particles, i.e., stronger averaging, one can observe that not only the standard deviation of the fluctuation decreases but also that the mean of the envelope changes significantly. This behavior is caused by the unbounded variance of the next-point estimator [*Lux and Kolbinger*, 1991, p. 386] in the probability summation method. Despite the fact that the energy density estimate converges toward the correct expectation [*Lux and Kolbinger*, 1991, p. 386] this bad convergence property renders the probability summation method inapplicable for strongly nonisotropic scattering.

2.4. Outline of the RadTrans Algorithm

[15] With the RadTrans algorithm we follow the approach of *Gusev and Abubakirov* [1996] and perform particle counting similar to *Yoshimoto* [2000]. In this case the radiance $I(\mathbf{n}, \mathbf{r})$ is modeled by the number density of particles $N(\mathbf{n}, \mathbf{r})$ that are located at position $\mathbf{r}$ and move into direction $\mathbf{n}$. Let us define $\Delta N(\mathbf{n}, \mathbf{r})$ as the change of particle density along the ray in direction $\mathbf{n}$, i.e., $\Delta N(\mathbf{n}, \mathbf{r}) = N(\mathbf{n}, \mathbf{r} + \mathbf{n}\Delta l) - N(\mathbf{n}, \mathbf{r})$. Noting that the differential operator on the left hand side of transfer equations (9), (10), and (11) is the total derivative along the ray [*Margerin*, 2005]:

$$\frac{d}{dl} \equiv \frac{d}{v dt} = \frac{\partial}{v \partial t} + \mathbf{n} \cdot \nabla, \qquad (12)$$

we can reformulate these equations in terms of $\Delta N(\mathbf{n}, \mathbf{r})$. This clarifies the relation between the transfer equations and the Monte Carlo modeling. We demonstrate this for the case of P intensity I^P. Substituting $\Delta N^P(\mathbf{n}, \mathbf{r})/\Delta l$ for $dI^P(\mathbf{n} \cdot \mathbf{r})/dl$ (according to equation (12)) in equation (9) and N^P for I^P we obtain after multiplication with Δl and division by N^P [cf. *Gusev and Abubakirov*, 1996]

$$\frac{\Delta N^P(\mathbf{n}, \mathbf{r})}{N^P(\mathbf{n}, \mathbf{r})} = -\Delta l \left(g_0^{PP} + g_0^{PS} \right) - \Delta l \frac{\omega}{\alpha_0^I Q^P}$$
$$+ \frac{\Delta l}{N(\mathbf{n}, \mathbf{r})} \left[\int_{4\pi} g^{PP}(\Theta) N^P(\mathbf{n}', \mathbf{r}) d\Omega_{n'} \right.$$
$$+ \int_{4\pi} g^{SP}(\Theta, \Phi) N_\theta^S(\mathbf{n}', \mathbf{r}) d\Omega_{n'}$$
$$\left. + \int_{4\pi} g^{SP}(\Theta, \Phi) N_\phi^S(\mathbf{n}', \mathbf{r}) d\Omega_{n'} \right]. \qquad (13)$$

This yields a probabilistic interpretation of equation (9). The left-hand side of equation (13) is the fractional change of the number of particles (that move in direction $\mathbf{n}$) on a path element Δl along a ray with direction $\mathbf{n}$. The right hand side has two terms representing loss of particles. The first term describes the fraction of particles that change direction upon scattering and leave the ray bundle. It depends on the total scattering coefficients $g_0^P = g_0^{PS} + g_0^{PP}$. The second term represents the fraction of particles that die off because of intrinsic attenuation. The last term of equation (13) represents the gain of particles. It depends on all particles at position $\mathbf{r}$ independent of their directions $\mathbf{n}'$ and polarizations. This gain is balanced by the scattering loss of rays with direction $\mathbf{n}'$. Thus, the first and last term of equation (13) are closely related and ensure the conservation of energy in the multiple scattering process. The third term contains all the details of the scattering process. After proper normalization, the differential and total scattering coefficients can be interpreted as probability density function. For instance, g_0^{PS}/g_0^P represents the probability that a particle initially in mode P continues its random walk in mode S after scattering. In a similar vein, we interpret $\Pi^{PS}(\Theta, \Phi) = g^{PS}(\Theta, \Phi)/4\pi g_0^{PS}$ as the angular probability distribution of particles that undergo P to S mode conversion upon scattering.

[16] During the Monte Carlo simulation a large number of particles has to be simulated successively to obtain a smooth estimate of $N(\mathbf{n}, \mathbf{r})$. The coordinate system in which the simulations are performed is explained in Appendix A. Appendix B describes how the particles are characterized in the simulation. After the particles are initialized, i.e., emitted from a source (Appendix C), they propagate through the medium during small time steps Δt in which they move a path Δl depending on the velocity. With a certain probability depending on the total scattering coefficients the particles are scattered into new directions (Appendix D) and with another probability they are eliminated or their weight is reduced because of intrinsic attenuation (Appendix E). If the particles are neither scattered nor eliminated they continue to propagate in their initial directions. The motion of the particles on the small path elements Δl is governed by ray theory which includes reflection/conversion and transmission at interfaces and bending of paths in the presence of velocity changes (Appendix F). The recording process is detailed in Appendix G. Appendix H describes how random numbers are generated from the given probability distributions for scattering angles and source radiation directions.

2.5. Performance

[17] The algorithm is implemented in C programming language. The simple overall structure of the code allows parallelization by splitting the loop over the particles. Using MPI it can be run in parallel on clusters of any size. The speed of the computation strongly depends on the parameters of the random medium and it is impossible to give general statements about the performance. The system requirements are defined by the size of the four-dimensional recording grid and the desired smoothness of the energy density estimates in space and time. Models for regional wave propagation over several hundred kilometers with a simulation length of several hundred seconds require memory of a couple of GB. In combination with inversion procedures that depend on the simulation of a large number of models, the application of this algorithm certainly requires the use of large computer clusters.

[18] The implementation has been tested and validated on the basis of three criteria.

[19] 1. Energy conservation for the Monte Carlo algorithm is verified by the invariance of the number of particles in the simulation. In the case of zero intrinsic absorption this is confirmed also in the presence of discontinuities.

[20] 2. Equipartition of P and S energy is verified by the convergence of the ratio between S and P energy towards the ratio of $2\alpha_0^3/\beta_0^3$ predicted asymptotically by radiative transfer theory [*Ryzhik et al.*, 1996].

[21] 3. Comparison with finite difference wave field calculations did not reveal any significant or systematic differences between the envelopes produced with our algorithm and ensemble averaged energy density envelopes produced with finite difference calculations in full space.

3. Structure and Evolution of the Pyrenees

[22] The geological setting and tectonics of the Pyrenean range (Figure 4) is characterized in the review paper by *Choukroune* [1992, p. 156] as "the Pyrenean belt cannot be easily compared to other belts and is probably unique in its unusual structural style and evolution." Therefore, we only present a simplified description which assumes a global
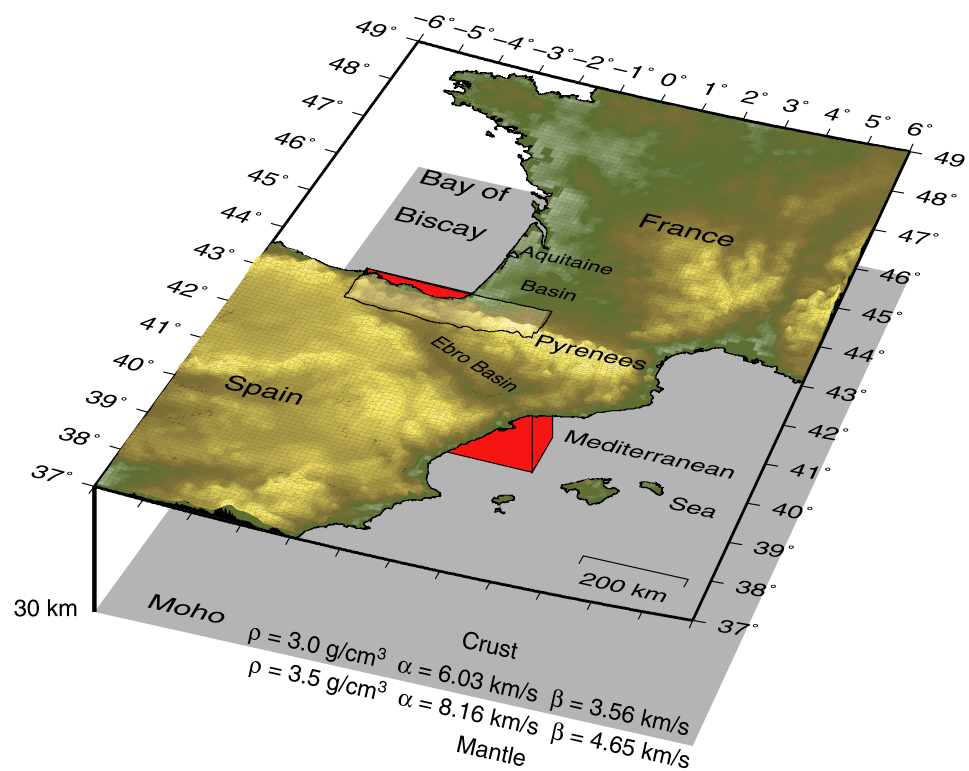
Figure 4. Map of the study area and illustration of the model that is used to explain the Lg blockage in the western Pyrenees. The gray plane and the red box depict the Moho and the region of increased heterogeneity, respectively. The parameters of the model are indicated. In the mantle the P wave velocity increases with depth by $d\alpha/dz = 300$ s^{-1}.

east-west orientation of the tectonic units resulting from the collision between the Iberian and European plates. The central part of the Pyrenees is formed by the Paleozoic Axial Zone (PAZ). This zone coincides with the main topographic expression of the Pyrenees. It is composed of Hercynian rocks that were reactivated during the Alpine orogeny. This zone is confined by the North Pyrenean Fault which marks the boundary of the North Pyrenean Zone (NPZ) to the north. The NPZ is composed of Mesozoic flysch deposits that are locally highly deformed and meta-morphosed. Some large Paleozoic outcrops form the North Pyrenean and the Basque massifs. Further north, the NPZ overrides the Aquitaine molasse basin along the North Pyrenean Frontal Thrust.

[23] Almost symmetrically, the South Pyrenean Zone (SPZ) confines the PAZ to the south. The SPZ is composed of Mesozoic and Cenozoic sediments. At the South Pyrenean Thrust, the SPZ overrides the Ebro Basin.

[24] Several seismic refraction and wide-angle reflection profiles revealed the Moho structure beneath the Pyrenees. There is a jump in Moho depth between the 50 km thick Iberian crust and the European crust which has a thickness between 29 and 35 km.

[25] Irrespective of this general north south structure that is common to the whole range there are variations along the axis of the Pyrenees. The compressional motion during the last 65 Ma is related to subduction of the Iberian lower crust beneath the Aquitaine basin in the eastern and central parts of the Pyrenees [*Souriau and Granet*, 1995]. The subduc-tion, first revealed by seismic tomography, was confirmed

by magnetotelluric measurements [*Pous et al.*, 1995] and gravity modeling [*Vacher and Souriau*, 2001]. In the western part the shortening has been accommodated in the crust.

[26] The lower crust in the western part of the NPZ has a much higher P wave velocity than the PAZ. *Daignières et al.* [1981] speculate that this difference is caused by intrusion of mantle material into the lower crust. This difference is not observed in the eastern part of the range. The emplacement of lower crustal blocks into the upper crust of the western Pyrenees has been detected by body wave tomography [*Souriau and Granet*, 1995], and gravity modeling combined with petrological information [*Vacher and Souriau*, 2001].

4. Data and Observations

[27] The geological variations in the Pyrenees along strike have an interesting manifestation in the attenuation properties of crustal waves. There is a pronounced differ-ence between the western part and the eastern and central parts of the Pyrenees. The western part strongly attenuates crustal waves [*Chazalon et al.*, 1993]. We illustrate this observation using data from the seismic network run by the French Atomic Energy Commission (CEA) and from the Spanish station PAB run by the Instituto Geográfico National, Spain. Figure 5 shows a map of the earthquakes and stations. The bold red line with black dots along the Pyrenees marks the axis used to sort the traces according to the place where the rays (blue lines) cross the Pyrenees. The
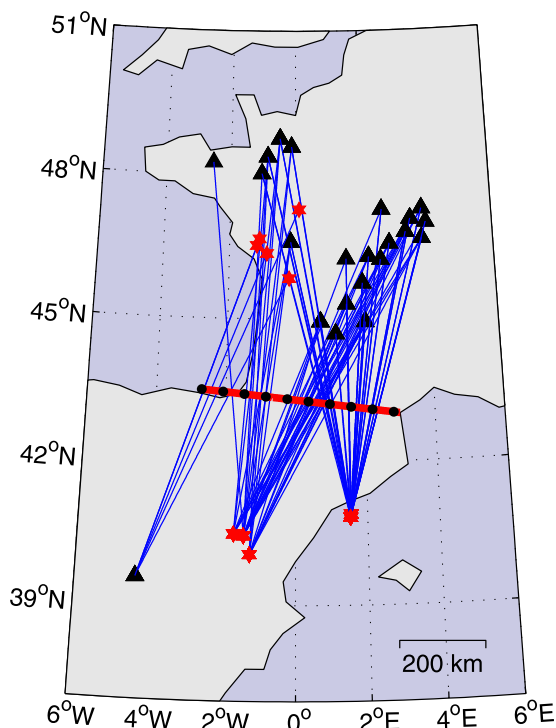
Figure 5. Map of the wave paths used in Figure 6. Black triangles indicate stations, and red stars indicate earthquakes. Red line with black dots shows the axis of the Pyrenees used to sort the traces in Figure 6. The black dots indicate 50 km intervals.

dots indicate 50 km distance intervals. The corresponding vertical velocity seismograms are shown in Figure 6. They are band-passed between 2 and 4 Hz, scaled to group velocity, normalized for their maximum and sorted for place

of intersection with the axis of the Pyrenees. The horizontal lines in Figure 6 indicate the velocities of the dominant regional seismic phases. These are the two crustal phases Pg (v_{Pg} = 6.03 km s^{-1}) and Sg (v_{Sg} = 3.56 km s^{-1}) and the two mantle phases Pn (v_{Pn} = 8.16 km s^{-1}) and Sn (v_{Sn} = 4.65 km s^{-1}). The velocities are taken from the velocity model of the CEA's geophysical laboratory (LDG).

[28] For wave paths that cross the eastern Pyrenees (east of the 250 km mark in Figure 6) seismograms are dominated by the crustal phases. The reverberations in the crust form an extended S wave of high amplitude, the Lg wave. The Sn arrival is barely visible and the Pn amplitude is small compared to the Pg phase. In the western part of the Pyrenees the situation is different. The traces that cross the Pyrenees west of the 200 km mark show almost no crustal phases. A strong Pn arrival is followed by Sn which usually has the highest amplitude. The Lg wave can hardly be recognized in the coda of the Sn phase. This strong attenuation of crustal phases, which is most obvious for the Lg waves is referred to as Lg blockage.

[29] Another illustration of the Lg blockage is presented in Figure 7. Figure 7a shows waveforms of six earthquakes that occurred north and south of the Pyrenees and that were recorded at the station SJPF inside the western Pyrenees. Figure 7b shows records of the same earthquakes made after the waves passed through the western Pyrenees. A map of events and stations is shown in Figure 8. The clear Pg and Lg waves in Figure 7a demonstrates that crustal phases are generated by the sources and travel from both sides toward the station inside the Pyrenees. Mantle phases are very weak. After passing through the Pyrenees the shape of the seismograms is again completely different as illustrated in Figure 7b. Except for events 1 and 6 where a small amplitude increase is visible at the arrival time of the Lg phase, there are no crustal phases. Using the interchangeability of source and receiver, this exactly reflects an
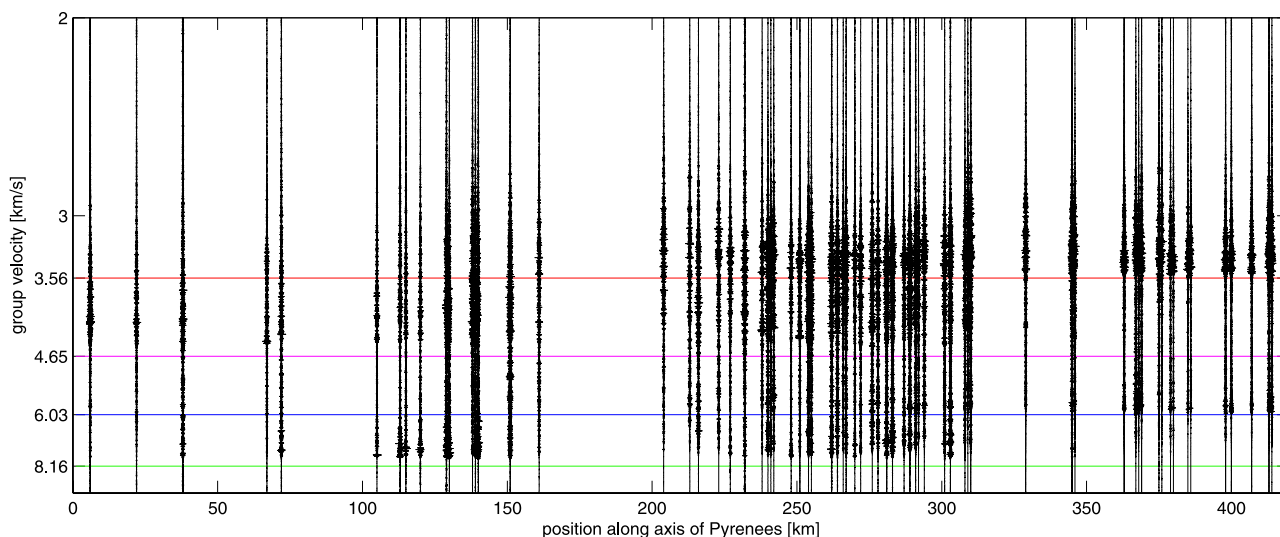

Figure 6. Collection of seismograms for wave paths through the Pyrenees. Traces are sorted according to the position of the intersection between their paths and the axis of the Pyrenees (red line in Figure 5). The traces are band-pass filtered between 2 and 4 Hz, normalized for their maximum, and scaled to group velocity. Horizontal lines indicate velocities of seismic phases: Pn (8.16 km s^{-1}), Pg (6.03 km s^{-1}), Sn (4.65 km s^{-1}), and Sg (3.56 km s^{-1}).
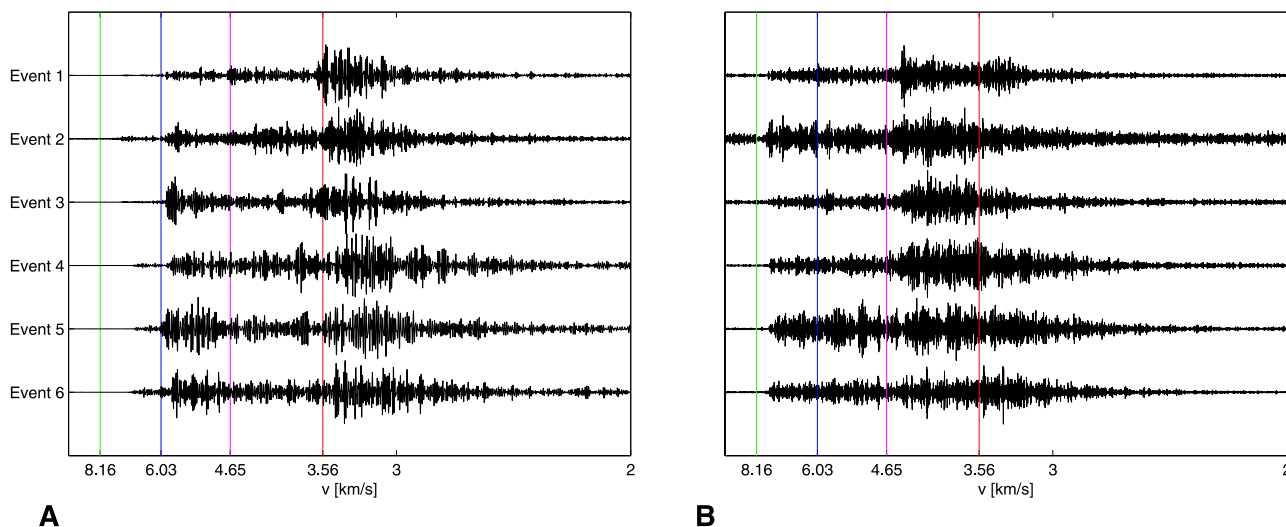
Figure 7. Seismograms of six earthquakes recorded within (a) the zone that blocks Lg waves and (b) recorded after the waves passed through this zone. A map showing the locations of the events and the stations is shown in Figure 8.

observation made by the analysts at the LDG. Some earthquakes in the western Pyrenees generate Lg waves that can be recorded at both sides of the range. But Lg waves that where generated outside the Pyrenees do not propagate through.

[30] To generate traces that represent the main characteristics of the undisturbed propagation through the eastern Pyrenees and the propagation through the western Pyrenees with blocked Lg waves, we use the following approach. We split the collection of traces in Figure 6 into groups according to the position of intersection between the raypath and the axis of the Pyrenees. For the first group we select traces that cross the Pyrenean axis between the 100 and 200 km marks. Epicentral distances of these traces ranges between 600 and 950 km. We exclude wave paths west of the 100 km mark to not be biased by paths through the Bay of Biscay. This group represents the propagation through the western Pyrenees. The second group that represents the eastern part is made up of paths east of the 300 km mark with epicentral distances between 500 and 850 km. The traces are band-passed between 2 and 4 Hz before the envelopes are computed with a Hilbert transform. The envelopes are normalized for their maximum, scaled to group velocity and stacked within each group. Figure 9 shows the resulting envelopes. These clearly show the characteristics of Lg blockage.

[31] Three mechanisms were proposed in the literature to explain similar observations of variable amplitude ratio between crustal and mantle phases.

[32] 1. The mantle phases propagate in a high Q medium with little attenuation whereas the crustal phases are more strongly attenuated [Bormann, 2002]. This generally causes a distance dependence of the amplitude ratio. Indeed the wave paths through the western Pyrenees are generally slightly longer than the paths in the east but there are records with equal or reversed distance relation. Also traces with the same source and equal epicentral distance show Lg blockage.

[33] 2. The radiation pattern of the source excites strong mantle phases and weak crustal phases [Bormann, 2002]. There are examples that confirm this situation but they seem rather rare. We use several earthquake sources to average the observation over different sources in order to minimize this effect.

[34] 3. The velocity structure in the western Pyrenees causes the Lg blockage. The last point is worth a more detailed discussion.
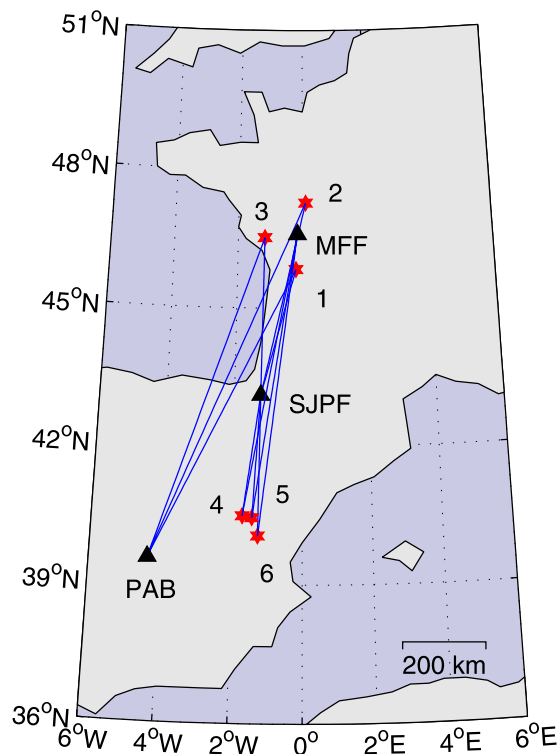

Figure 8. Map of the study area with wave paths used in Figure 7. Black triangles indicate stations, and red stars indicate earthquakes.
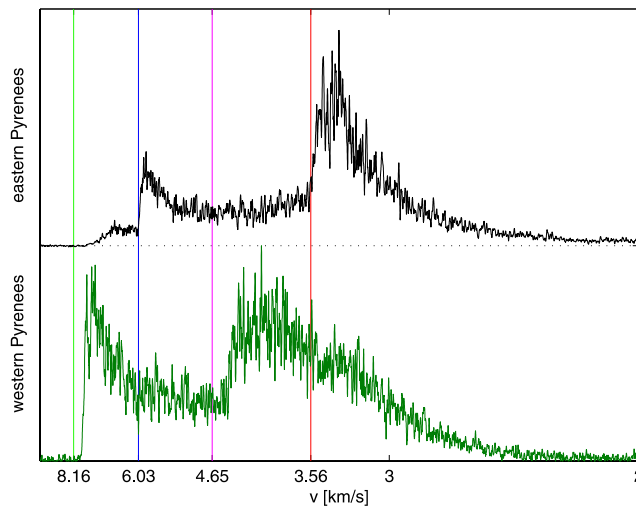
Figure 9. Reference traces from the eastern and western Pyrenees. Vertical lines indicate arrival times of seismic phases. The upper black trace represents undisturbed propagation through the eastern Pyrenees. It shows clear arrivals of crustal phases. The bottom trace represents wave paths through the western Pyrenees. Here the crustal phases are attenuated and only the mantle phases show clear arrivals.

[35] The sensitivity of Lg waves to crustal structure is known from the extinction of this phase when passing through oceanic crust. Lg blockage has also been reported from the Barents Sea [*Baumgardt*, 2001], eastern Mediterranean, the Caspian Sea, the Black Sea, the Red Sea [*McNamara and Walter*, 2001; *Rodgers et al.*, 1997] and the Lingurian Sea [*Shapiro et al.*, 1996] and the Alpine range [*Campillo et al.*, 1993]. In most of these cases the attenuation is caused by soft marine sediments. They form a layer of very low shear velocity and high attenuation that traps the energy which propagates in the crust. The extinction of Lg waves across sedimentary basins was modeled by *Shapiro et al.* [1996]. They showed that the large-scale velocity structure explains the gross features of the Lg extinction. The blockage of Lg waves across mountain ranges such as the Alps and the Pyrenees is of a different nature. There are sedimentary basins north and south of the Pyrenees but they are not comparable in depth, extent and velocity to the marine situations. For the specific situation of the western Pyrenean crust, *Chazalon et al.* [1993] modeled the wave propagation with a realistic velocity model including the Moho jump and large-scale, high-velocity obstacles in the upper crust. *Chazalon et al.* [1993] conclude from their modeling that neither the Moho jump nor the detailed crustal velocity structure can cause the observed attenuation. The inability of the Moho jump to cause the Lg blockage is supported by the observed Lg propagation through the eastern Pyrenees where the Moho jump is also present.

[36] In summary, the extinction of Lg waves displayed in Figure 6 reflects intrinsic properties of the propagation medium and is due neither to the sources nor to the velocity structure. There is no satisfactory explanation for the Lg

blockage by the Pyrenees or the Alps. It was speculated by *Chazalon et al.* [1993] that the increased scattering by small-scale heterogeneities in the western Pyrenean crust causes the attenuation of crustal phases.

5. Modeling

[37] To test this hypothesis, the energy propagation through the Pyrenees is modeled with elastic radiative transfer theory (RTT). This theory in the acoustic approximation was applied in a number of studies focusing on the separation of intrinsic and scattering attenuation in simple half-space models [e.g., *Hoshiba*, 1991; *Fehler et al.*, 1992; *Gusev and Abubakirov*, 1996]. The Lg coda in central France was modeled by *Lacombe et al.* [2003] on the basis of acoustic radiative transfer theory in a model that consists of a layer overlying a half-space. Here the elastic version of RTT is used in a complex geometrical model that consists of a scattering layer over a scattering half-space with a vertical velocity gradient. Additionally a cuboid body with different scattering and attenuation properties is included in the crustal layer to model the local effect of the western Pyrenean crust. Let us emphasize that the main focus is not on the estimation of precise parameters of the model. Instead we try to present a conceptual model to explain the phenomenon of Lg blockage in the Pyrenees.

[38] The velocity model that is used for the simulation is illustrated in Figure 4. It is based on the model of the LDG and consists of a constant velocity layer for the crust and a half-space with constant vertical velocity gradient for the mantle, separated by the Moho at 30 km depth. Velocity and density values for the crust and the top of the mantle are given in Figure 4. The velocity gradient for P waves is $1/300$ s^{-1} which is an approximate average of the velocity profile in the uppermost 600 km of the mantle in the Preliminary Reference Earth Model (PREM) [*Dziewonski and Anderson*, 1981]. The velocity ratio γ is constant throughout the mantle. Small-scale heterogeneities are described by an exponential autocorrelation function (equation (D5)) with variance ε and correlation length a. The scattering properties in the crust and mantle are different but uniform' that is, they do not vary with depth. Intrinsic attenuation is described phenomenologically by quality factors. To fix the ratio between the quality factor of P and S waves, we assume that intrinsic attenuation is limited to shearing which implies $^I Q^P = 9/4 ^I Q^S$ [see, e.g., *Shearer*, 1999, p. 114].

[39] The cuboid body that is included in the crust beneath the western Pyrenees has the same mean velocities and density as the surrounding crust but differs in the scattering and attenuation properties. The body extends from the surface down to the Moho and has width of 100 km perpendicular to the axis of the mountain range (Figure 4). This width corresponds to the topographic expression of the Pyrenees. In the following we try to determine whether or not the attenuation and scattering properties of this body can account for the Lg blockage. Since the reference traces are the result of averaging over different earthquakes, we model the source with an isotropic radiation pattern. Assuming a point source in a Poisson solid we fix the proportion of radiated P and S energy at 96% S energy and 4% P energy
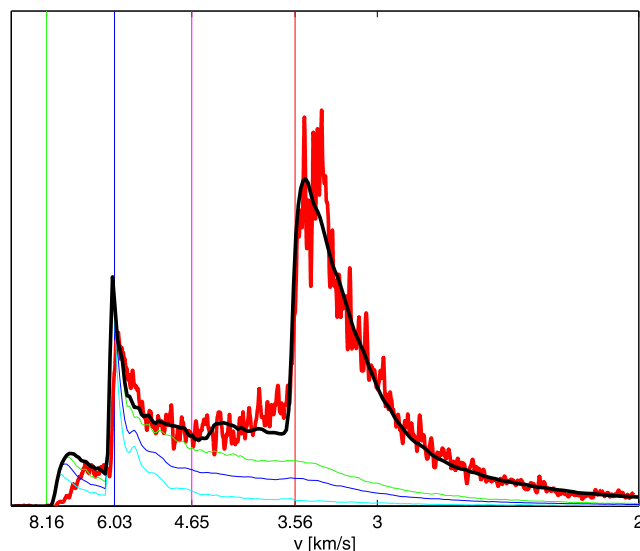
Figure 10. Simulation results for the undisturbed propagation through the eastern Pyrenees. Bold red and black traces represent data and model, respectively. Thin traces indicate types of energy. Cyan trace shows radiated P energy that arrives at the receiver as P energy. The difference between the cyan and blue traces shows radiated P energy that arrives as S energy. The difference between blue and green traces shows radiated S energy that arrives as P. Radiated S energy that arrives as S is indicated by the difference between the green and the black trace. Vertical lines indicate arrival times of seismic phases.

(equation (C1)). Please refer to *Shearer and Earle* [2008] for a discussion of this choice.

6. Inversion

[40] The goal of the nonlinear inversion process is to find scattering and attenuation parameters for the crust, mantle and Pyrenean body that result in energy density traces which fit the eastern and western reference traces. Although some of the parameters may be estimated independently, the whole model has 9 free parameters, the fluctuation strength ε the correlation length a and the quality factor ^IQ of the three different units. Because of the high number of free parameters we apply a genetic algorithm [*Mitchell*, 1996] for the inversion. Parameters are preferably tested in the ranges $0.003 < \epsilon < 0.3$, $0.1 < a < 100$ km, and $50 < ^IQ^P < 5000$. The principal elements of the algorithm are recombination of the parameters of the fittest models and mutation to maintain diversity. Recombination ensures that the parameter space is densely explored in the surroundings of successful models. Fitness of the models is linked to the misfit between the model and the reference trace. The misfit is the sample wise average of the absolute value of the difference between the logarithm of the model envelope and the logarithm of the reference. This is the L1 norm of the difference between the logarithmic traces. It ensures that the low-amplitude coda has similar weight for the misfit calculation as the high-amplitude direct arrivals and is not too sensitive to fluctuations in the data and the simulated envelopes.

6.1. Undisturbed Case

[41] In a first inversion we estimate the parameters of the background model. For this, the crustal phases of the eastern reference trace are fitted by adjusting the parameters a, ε and Q of the crust in a model that has a transparent (no scattering) and nonattenuating mantle and no additional body. The lapse time windows used to calculate the misfit in this inversion step are the Pg window between the Pg arrival and the Sn arrival and the S coda from the Sg arrival until a group velocity of 2 km s^{-1} to the generation of the reference traces we stack RMS envelopes in a certain distance range after scaling to equal group velocity. For comparison with the eastern reference trace we stack records between 500 and 800 km distance from the source.

[42] With this model of the crust we invert the western reference trace for scattering and attenuation properties of the mantle. Because of the blockage of the crustal phases the wave paths through the western Pyrenees offer the interesting possibility to estimate mantle properties relatively independent of the crust. In this inversion step we use time windows that contain the mantle phases, i.e., the Pn window between the Pn and the Pg arrivals and the Sn window between the Sn and the Sg arrivals. RMS envelopes between 600 and 900 km are stacked in this case to account for the slightly longer wave paths through the western Pyrenees. The results of this inversion step are not well determined and a relatively wide range of values for the parameters ε, a and ^IQ in the mantle can be used to fit the reference trace. We therefore fixed the parameter for the fluctuation strength and correlation length of the mantle to $\varepsilon = 0.02$ and $a = 2$ km. This resulted in the quality factors $^IQ^P = 1070$ and $^IQ^S = 475$.

[43] With these new parameters for the mantle we reinverted the eastern reference trace for the crustal properties because the increased scattering in the mantle changed the amount of energy that returns from the mantle into the crust. This process raised the level of the coda and required changes of the parameters in the crust. The final parameters of the crustal material are $\varepsilon = 0.021$, $a = 0.77$ km, $^IQ^P = 1400$ and $^IQ^S = 623$.

[44] Figure 10 shows the result of this inversion. The general fit of the model is fairly good. Especially the decay of the S coda is well fitted. The kink in the S coda envelope shortly after 3 km s^{-1} originates from the reverberations in the crust. It marks the end of the Lg wave train which is well modeled by the algorithm. The fit is less good for the P coda and the Pn phase. The deviation from the shape of the Pn arrival is due to the fact that we estimated the mantle properties from the western reference trace. We can better fit the Pn phase with stronger scattering in the mantle but then the impulsive shape of the mantle phases in the western reference trace cannot be reproduced. In fact, this is an indication for slightly different mantle properties under the eastern and western Pyrenees.

6.2. Disturbed Case

[45] To model the Lg blockage, we use the background model described in section 6.1 and include an extra body (see Figure 4) with different scattering and attenuation
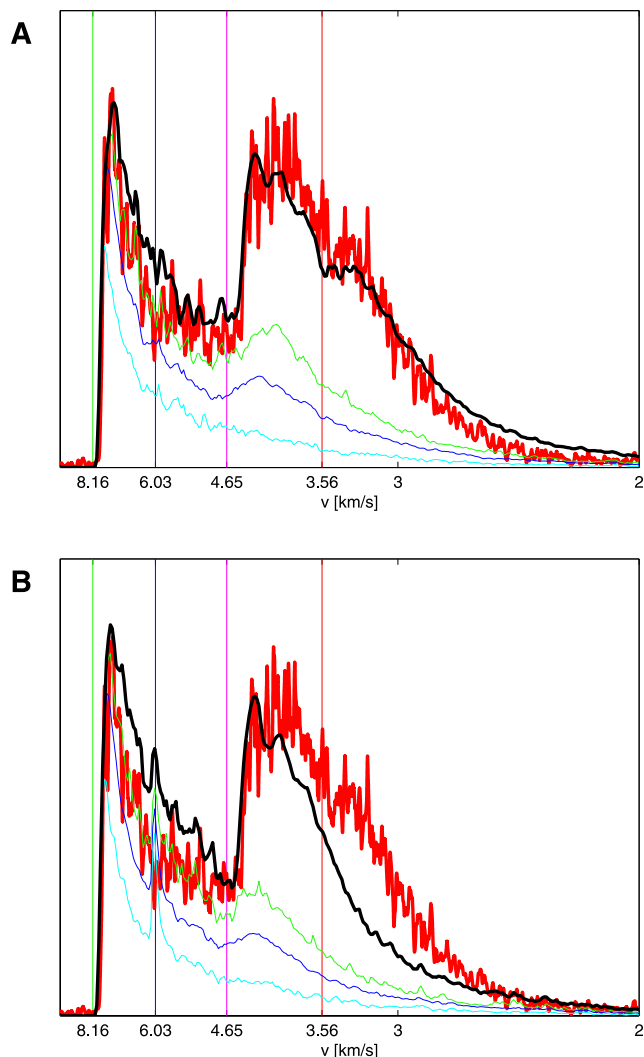
Figure 12. Simulation results for propagation through the western Pyrenees with both stronger scattering and increased attenuation. For explanations, see Figure 10.

Figure 11. Simulation results for propagation through the western Pyrenees with (a) stronger scattering and (b) increased attenuation. For explanations, see Figure 10.

properties. Only the properties of this body are varied here. To speed up the Monte Carlo simulations, we slightly modify this model to enforce cylindrical symmetry which allows better averaging. In the modified model the cuboid attenuating body is replaced by a cylinder ring centered at the source. The radius of the inner boundary is 300 km and the width is 100 km. We verified that the effect of this modification on the inversion is very weak.

[46] Three different variants of the model are used for the inversion. In the first variant the fluctuation strength of the small-scale heterogeneities is adjusted to fit the western reference trace. The intrinsic attenuation and the correlation length in the inclusion are equal to the surrounding crust. With $\varepsilon = 11\%$ the best fit is obtained (Figure 11a). The general shape of the data is reasonably well fitted. The strong scattering in the inclusion efficiently attenuates the crustal phases. There is no Pg arrival and the Sg phase is only visible as a small bump in the Sn coda. This shows that scattering is a good candidate to explain the Lg blockage in the Pyrenees. However, there is some mismatch between
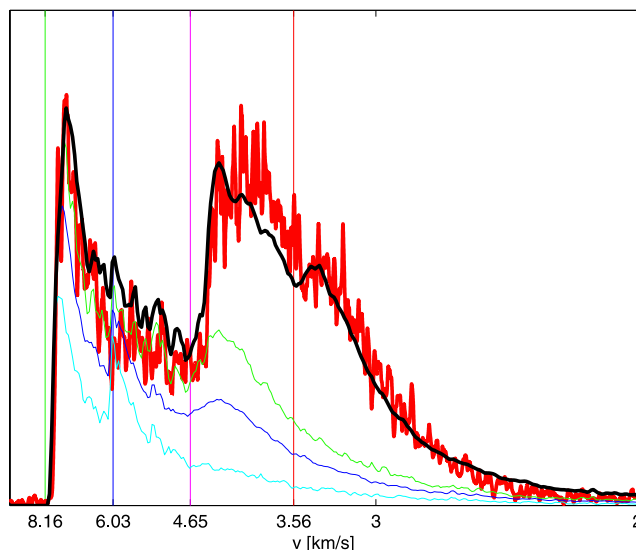
this model and the data in the S coda as there is too much energy in this part of the simulated envelope.

[47] In a second variant of the model we assume that the Lg blockage is caused by intrinsic attenuation. The inclusion has the same scattering properties as the normal crust but variable ^IQ values. Again the ratio between $^IQ^P$ and $^IQ^S$ is fixed at 9/4. The best fit is obtained for $^IQ^P = 86$ and $^IQ^S = 38$. These values are extremely low. Figure 11b shows the results of the model. The fit is worse compared to the fit achieved by changing the scattering strength. The S coda of the model is much too low but there is still Pg energy that propagates through the inclusion. It is impossible to attenuate strongly the Pg phase, while increasing the energy level in the S coda. Leaving the $^IQ^P/^IQ^S$ ratio unconstrained would allow us to obtain a much better fit. But this would require much stronger P than S attenuation which is unrealistic. This shows that intrinsic attenuation alone does not suffice to explain the extinction of Lg waves.

[48] In the third model we allow for variable scattering and attenuation in the inclusion. With this model the best fit is obtained as illustrated in Figure 12. The parameters are

Table 1. Parameters of the Final Model Used to Explain the Phenomenon of Lg Blockage by the Pyrenees[a]

	$^IQ^P$	$^IQ^S$	ε	a (km)	l_S^* (km)
Crust	1400 (1350)	623 (600)	2.1%	0.77	761
Mantle	1070 (321)	475 (143)	2.0%	2.0	1529
Pyrenean body	402	179	7.2%	0.77	65

[a]Values are shown for the intrinsic quality factor of P waves ($^IQ^P$) and S waves ($^IQ^S$), the fluctuation strength (ε) and the correlation length (a) of the small scale velocity fluctuations, and the transport mean free path l_S^* [*Turner*, 1998]. The values of ε and a in the mantle are fixed by hand. The correlation length a of the Pyrenean body is assumed to equal the correlation length of the surrounding crustal material. Values in parentheses show representative numbers of the PREM [*Dziewonski and Anderson*, 1981]. The 761 km transport mean free path can be compared to the mean free path of 690 km obtained by *Sens-Schönfelder and Wegler* [2006] with an isotropic scattering model for the German crust.
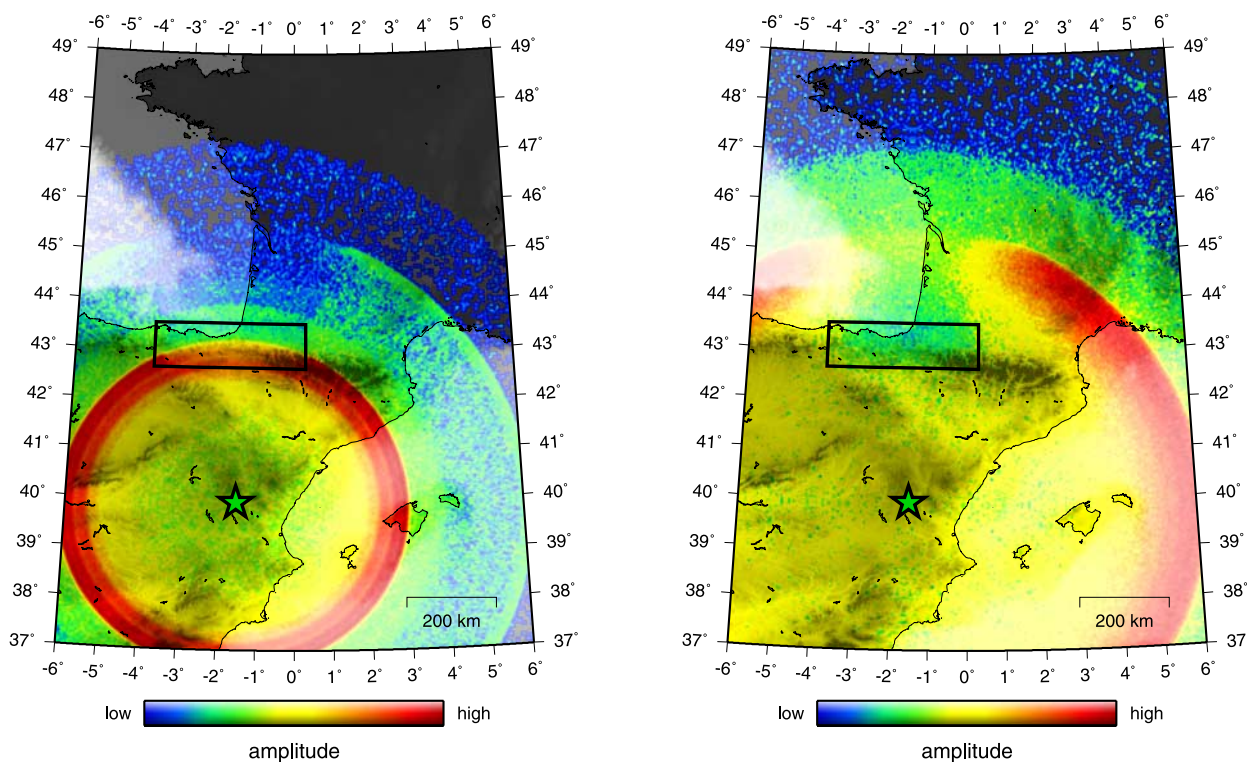
Figure 13. Snapshots of the energy density field at (a) 105 s and (b) 180 s lapse time for an earthquake in Spain. Green star and black box indicate the epicenter and the disturbed body beneath the western Pyrenees, respectively. The linear color scale indicates the square root of seismogram envelopes, i.e., fourth root of energy density. Relief is indicated by brightness. The shadowing effect of the medium in the box can be seen for the Pg wave (Figure 13a) and for the Lg wave (Figure 13b).

$^I Q^P = 402$, $^I Q^S = 179$ and $\varepsilon = 7.7\%$. With these parameters the two dominant crustal phases can be appropriately attenuated. The Pg phase is weak enough not to stick out of the Pn coda and, at the same time, the small signature of the Lg wave is reproduced. Also the amplitude ratio between the Pn and Sn phases is reasonable. For this model, all the parameters are listed in Table 1.

[49] We conclude that strong attenuation alone cannot explain the observation of Lg blockage in the Pyrenees. Increased scattering seems an essential ingredient of this phenomenon but is not able to explain all the details of the observation. The best results are obtained with a combination of increased scattering and stronger intrinsic attenuation.

7. Discussion

[50] Compared to the waveform modeling by *Chazalon et al.* [1993], we use a fairly simple structural model that consists of a flat layer over an infinite half-space. It does neither contain the deterministic velocity structure inside the crust nor the Moho topography. In spite of these limitations, the shape of the seismogram envelopes in the eastern Pyrenees can be reproduced. Including an extra body with stronger scattering and attenuation, the energy transport can be influenced to reproduce the seismogram envelopes that are observed after propagation through the western Pyrenees. For the final parameters we illustrate the energy field

with two snapshots of the simulations in Figures 13a and 13b. Figures 13a and 13b illustrate the shadowing effect of the inclusion (marked by the black box) for crustal waves in the western Pyrenees. The epicenter is indicated by the star. The linear color scale represents the square root of seismogram envelopes, i.e., the fourth root of energy to optimally use the color scale. Figure 13a displays the energy distribution at a lapse time of 105 s. At this time the P phases already passed the Pyrenees. The Pn mantle phase which propagated north to about 47°N is unaffected by the Pyrenees. Its energy is low compared to the other phases and the speckle reflect the statistical fluctuations of the Monte Carlo simulations. P energy that propagated in the crust forms the Pg phase which is limited to the north at about 45° latitude. This phase experienced strong attenuation in the western Pyrenean crust. The Sn wavefront just leaves the box and the Lg wave enters it. Figure 13b shows the situation at 180 s lapse time. The P wavefronts already left the map and the Sn and Lg wavefront extend north to about 47°N and 45°N, respectively. Again the mantle phase is continuous behind the Pyrenees whereas the crustal Lg shows a gap behind the western Pyrenees. The almost homogeneous color behind the Lg wave illustrates the spatial homogenization of energy density in the seismic coda.

[51] The simulations show a consistent picture of the phenomenon of Lg blockage. They are obtained with model parameters (see Table 1) that appear to be reasonable. The

parameters for the crust match existing estimates quite well. The quality factor of intrinsic S wave attenuation (623) is close to the value of 600 given in the PREM [*Dziewonski and Anderson*, 1981]. It is also comparable to the estimate of 770 obtained with the isotropic half-space model by *Sens-Schönfelder and Wegler* [2006]. The scattering properties are best described by the S wave transport mean free path of 761 km. Again this is close to the 690 km found by *Sens-Schönfelder and Wegler* [2006]. The parameters for the mantle are not well constrained and are adjusted in an ad hoc fashion. Note that the transport mean free path must be larger in the mantle than in the crust in order to fit the impulsive Pn arrival of the western reference trace. The medium that causes the Lg blockage is described by a transport mean free path of 65 km which is in the range of parameters estimated in other regions of the world [cf. *Sato and Fehler*, 1998].

[52] In order to appreciate the degree of scattering anisotropy, we have calculated the weighted average of the cosine of the scattering angle $\langle\cos(\Theta)\rangle$ for the P to P and S to S scattering process. These parameters are denoted by $g_{c,m}^{SS}$, $g_{c,m}^{SS}$, where the subscripts c and m stand for crust and mantle, respectively. There is a strong tendency for scattering anisotropy in both the crust and mantle: $g_c^{SS} = 0.91$, $g_m^{SS} = 0.97$, $g_c^{PP} = 0.84$, $g_m^{PP} = 0.94$. In spite of larger wave speeds and hence longer wavelengths, the mantle shows stronger scattering anisotropy than the crust due to the increase of the correlation length.

[53] The attenuation with a S wave quality factor of 179 is rather strong for crustal material [cf. *Sato and Fehler*, 1998]. But this is in correspondence with implication of the seismicity distribution. The intrusive bodies of lower crustal material of which two were identified in the seismically active upper crust of the western Pyrenees are seismically quiet [*Souriau et al.*, 2001]. *Souriau et al.* [2001] proposed that this is due to the more ductile lower crust material which most likely shows stronger attenuation.

[54] Please note that no confidence intervals are given for the model parameters and we do not put any emphasis on these values because their exact determination is not the scope of this study. Also the geometrical parameters of the model like the extent of the perturbed zone, the depth of the Moho or the velocity gradient in the mantle should not be considered as precise estimates. It is assumed that the mantle phases Pn and Sn are made up of energy that left the crust through the Moho and returned after traveling through the mantle according to ray theory. Energy that travels as interface wave along the discontinuity is neglected just like surface waves. It might thus be possible to find models with different parameters that similarly fit the data. However, the neglected effects are expected to have a small effect on the Lg blockage and will thus not influence the general results and conclusions of this study. Our work presents a conceptual model with realistic parameters that explains the so far unexplained phenomenon of Lg blockage in the western Pyrenees.

8. Conclusions

[55] With elastic Monte Carlo simulations in a model with deterministic velocity structure and statistically described small-scale heterogeneities it is possible to calculate seismogram envelopes of crustal earthquake records including mantle phases and coda. Including an additional body with different scattering and attenuation properties this model provides an explanation for the Lg blockage by the Pyrenees. To coincide with the geographical situation, this body should be located under the western Pyrenees. This region is characterized by strong deformation. The crust was squeezed during the compressional phase that led to the formation of the Pyrenees. There is geological and geophysical evidence for material exchange between the different depths. Mantle material is lifted to lower crustal depths and lower crust material can be found in the upper crust. These observations appear to be consistent with increased heterogeneity as suggested by our model because the uplift may have been associated with some kind of 'stirring' that generated small-scale velocity contrasts and the highly heterogeneous lower crust material now extents close to the surface. In the eastern and central Pyrenees the shortening led to subduction of the Iberian lower crust beneath the European plate. This process reduced the deformation in the crust. We speculate that the strong deformation in the western Pyrenees increased heterogeneity and intrinsic attenuation in the crust. These material changes cause the attenuation of crustal phases known as Lg blockage. The model might also be applicable to the situation in the western Alps [*Campillo et al.*, 1993].

Appendix A: Coordinate System

[56] For the recording and the propagation of the particles it is convenient to describe their position and velocity in Cartesian coordinates. The treatment of reflection, transmission and conversion at horizontal interfaces and the treatment of the scattering processes requires knowledge of the polar and azimuthal angles of the propagation direction. The orientation of the sources and the position of the seismic station in turn requires a relation to geographical coordinates. In Figure 2 the relations between the Cartesian, the polar, and the geographical coordinates as they are used in the algorithm are illustrated. The Cartesian system is oriented with the Z coordinate increasing downward. X and Y point northward and eastward, respectively. The azimuthal angle ϕ is measured eastward from north and the polar angle θ is measured from the vertical downward.

Appendix B: Description of a Particle

[57] For a complete description of a particle the following parameters are needed: (1) mode of the particle, (2) coordinates in space and time (x, y, z, t), (3) velocity vector (v_x, v_y, v_z), and (4) Stokes vector $(I^P, I_\theta^S, I_\phi^S, U, V)$ describing the polarization. For convenience, the following parameters are stored additionally: (1) direction of velocity vector in polar coordinates (v_θ, v_ϕ) and (2) polarization angle ψ, defined as the angle between the polarization axis of a linearly polarized S wave and the vertical plane that contains the raypath. Knowledge of the propagation direction in polar coordinates and of the polarization angle, is useful for the treatment of interface reflections/conversions/transmissions

and the transformation of scattering angles from the local to the global coordinate system.

Appendix C: Particle Emission From the Source

[58] To launch particles from the source, a probabilistic description of the radiation pattern for each polarization is needed. The probability density function (pdf) of angular variables is proportional to the square of the far field radiation pattern of a double couple source as given for example by *Sato and Fehler* [1998]. In the modeling of the Lg blockage presented in section 3 we perform an average over several independent sources with various orientations which we simply model with an isotropic source. The ratio between radiated P energy (W^P) and S energy (W^S), i.e., the ratio between the number of emitted P and S wave particles is obtained from the model for a point shear dislocation [cf. *Sato and Fehler*, 1998, p. 149]

$$\frac{W^S}{W^P} = \frac{3}{2}\gamma^5, \tag{C1}$$

where γ denotes the ratio between the P and S velocities at the source.

Appendix D: Scattering

[59] The most interesting and complicated part of the algorithm is the simulation of scattering of elastic vector waves by distributed heterogeneities. To calculate the scattering pattern in the Born approximation, we follow the derivation by *Sato and Fehler* [1998].

D1. Random Medium

[60] Let us assume that a certain property v of the medium is not constant in space but depends on position $\mathbf{x}$. This property may be the wave velocity, the density or a Lamé coefficient. The field $v(\mathbf{x})$ can be written as the sum of a background mean field v_0 and a perturbation δv:

$$v(\mathbf{x}) = v_0 + \delta v(\mathbf{x}) = v_0[1 + \xi(\mathbf{x})], \tag{D1}$$

where $\xi(\mathbf{x})$ is the fractional fluctuation. $v_0(\mathbf{x})$ is chosen such that the average, denoted by $\langle \ldots \rangle$, of an ensemble of heterogeneous media is

$$v_0 = \langle v(\mathbf{x}) \rangle, \text{ or } \langle \xi(\mathbf{x}) \rangle = 0. \tag{D2}$$

Note that v_0 may vary for instance with depth as is the case for a stratified medium. The random function $\xi(\mathbf{x})$ is best described by its spectral properties. For this purpose, we introduce the autocorrelation function (ACF) as

$$R(\mathbf{x}) \equiv \langle \xi(\mathbf{y})\xi(\mathbf{y} + \mathbf{x}) \rangle. \tag{D3}$$

In the following it is assumed that the random function ξ is isotropic and homogeneous which means that R does only depend on the distance r between $\mathbf{y}$ and $\mathbf{x}$ ($r \equiv |\mathbf{y} - \mathbf{x}|$).

[61] The strength of the fluctuations is given by the mean square fractional fluctuation or variance

$$\varepsilon^2 \equiv R(0) = \left\langle \xi(\mathbf{x})^2 \right\rangle \tag{D4}$$

and the typical scale of the fluctuations is characterized by the correlation length a. The Fourier transform of the ACF R gives the power spectral density function (PSD). For isotropic and homogeneous random media the PSD is a function of the magnitude of the wave number vector $m \equiv |\mathbf{m}|$. We adopt the popular ACF of exponential form:

$$R(r) = \varepsilon^2 e^{-r/a} \text{ and } PSD(m) = \frac{8\pi\varepsilon^2 a^3}{(1 + a^2 m^2)^2} \tag{D5}$$

D2. Scattering Coefficients

[62] Scattering at distributed heterogeneities in a random medium can be described by the scattering coefficients. The formal derivation starting from the wave equation in a random medium is given by *Sato and Fehler* [1998, pp. 95–105]. Beginning with a scalar wave of unit amplitude and angular frequency ω incident on an inhomogeneity which is localized at the origin one can define the scattering amplitude F as

$$u_{sc}(\mathbf{x}, t) = \frac{e^{i(kr-\omega t)}}{r} F. \tag{D6}$$

It relates the amplitude of a wave $u_{sc}(\mathbf{x}, t)$ that is scattered in a certain direction to the amplitude of the incident wave. For elastic waves there is one scattering amplitude for each type of scattering event. The ratio between the amount of energy scattered in a given element of solid angle to the incident energy flux (J_0) defines the differential scattering cross section:

$$\frac{d\sigma^{AB}}{d\Omega} \equiv \frac{J_{sc}r^2}{J_0} = \frac{v_B}{v_A}\left|F^{AB}\right|^2. \tag{D7}$$

The superscripts A and B stand for either P or S and allow us to keep track of the scattering process. v_A and v_B are the mean local velocities of the respective modes. If the inhomogeneities are not localized but distributed over a larger volume the scattering coefficient may be defined as 4π times the ensemble average of the scattering cross section of a region of size L:

$$g^{AB} \equiv 4\pi \frac{1}{L^3}\left\langle \frac{d\sigma^{AB}}{d\Omega} \right\rangle = 4\pi \frac{v_B}{v_A L^3}\left\langle \left|F^{AB}\right|^2 \right\rangle. \tag{D8}$$

Thus, the scattering coefficients relate the incident energy flux to the angular-dependent scattered energy flux from distributed heterogeneities in a region of unit size.

[63] To simplify the expressions for the scattering coefficients, it is assumed that the fluctuations of the wave velocities are equal. They are correlated with the mass density of rock as stated by Birch's law [*Birch*, 1961]. These correlations reduce the fluctuations to one single fractional fluctuation that is common to the wave velocities and the mass density.

$$\xi(\mathbf{x}) \equiv \frac{\delta\alpha(\mathbf{x})}{\alpha_0} = \frac{\delta\beta(\mathbf{x})}{\beta_0} = \frac{1}{\nu}\frac{\delta\rho(\mathbf{x})}{\rho_0} \tag{D9}$$

where α and β are the velocities of P and S waves, respectively, and ρ is the mass density. The parameter ν ranges between $0.78 < \nu < 0.8$ in typical lithosphere [*Sato and Fehler*, 1998, p. 101].

[64] In spherical coordinates (Θ, Φ) the scattering coefficients are given by *Sato and Fehler* [1998, p. 104]:

$$g^{PP}(\Theta) = \frac{l^4}{4\pi} \left| X^{PP}(\Theta) \right|^2 PSD\left(\frac{2l}{\gamma_0} \sin\left(\frac{\Theta}{2}\right) \right), \quad (D10)$$

$$g^{PS}(\Theta) = \frac{1}{\gamma_0} \frac{l^4}{4\pi} \left| X^{PS}(\Theta) \right|^2 PSD\left(\frac{l}{\gamma_0} \sqrt{1 + \gamma_0^2 - 2\gamma_0 \cos(\Theta)} \right), \quad (D11)$$

$$g^{SP}(\Theta, \Phi) = \gamma_0 \frac{l^4}{4\pi} \left| X^{SP}(\Theta, \Phi) \right|^2 PSD\left(\frac{l}{\gamma_0} \sqrt{1 + \gamma_0^2 - 2\gamma_0 \cos(\Theta)} \right), \quad (D12)$$

$$g_l^{SS}(\Theta, \Phi) = \frac{l^4}{4\pi} \left| X_l^{SS}(\Theta, \Phi) \right|^2 PSD\left(2l \sin\left(\frac{\Theta}{2}\right) \right), \quad (D13)$$

$$g_r^{SS}(\Theta, \Phi) = \frac{l^4}{4\pi} \left| X_r^{SS}(\Theta, \Phi) \right|^2 PSD\left(2l \sin\left(\frac{\Theta}{2}\right) \right). \quad (D14)$$

Θ measures the angle between the initial direction and the direction of the scattered particle. This angle is usually called scattering angle. Φ measures the angle between the polarization direction of the incident particle and the scattering plane spanned by the incident and scattered directions. Superscripts indicate the type of scattering. *SP* for example stands for the scattering of an S wave into a P wave. Subscripts r and l indicate the polarization of the scattered particle with respect to the scattering plane; r and l stand for perpendicular (normal to scattering plane) and parallel (in the scattering plane), respectively. This distinction is necessary for *SS* scattering only, since the polarization of P waves is always longitudinal and S waves generated by scattering from P waves are polarized in the scattering plane. The argument of the power spectral density function is the so-called exchange wave number expressed in terms of the scattering angle and the S wave number l. The terms denoted by X are the basic scattering patterns. They are the same for all types of isotropic elastic media. Modifications of the angular patterns of the scattering coefficients are solely introduced by the power spectrum of the heterogeneities. The scattering patterns are given by *Sato and Fehler* [1998, p. 102]:

$$X^{PP}(\Theta) = \frac{1}{\gamma_0} \left[\nu \left(-1 + \cos(\Theta) + \frac{2}{\gamma_0^2} \sin^2(\Theta) \right) - 2 + \frac{4}{\gamma_0^2} \sin^2(\Theta) \right], \quad (D15)$$

$$X^{PS}(\Theta) = -\sin(\Theta) \left[\nu \left(1 - \frac{2}{\gamma_0} \cos(\Theta) \right) - \frac{4}{\gamma_0} \cos(\Theta) \right], \quad (D16)$$

$$X^{SP}(\Theta, \Phi) = \frac{1}{\gamma_0^2} \sin(\Theta) \cos(\Phi) \left[\nu \left(1 - \frac{2}{\gamma_0} \cos(\Theta) \right) - \frac{4}{\gamma_0} \cos(\Theta) \right], \quad (D17)$$

$$X_l^{SS}(\Theta, \Phi) = \cos(\Phi) [\nu(\cos(\Theta) - \cos(2\Theta)) - 2\cos(2\Theta)], \quad (D18)$$

$$X_r^{SS}(\Theta, \Phi) = \sin(\Phi) [\nu(\cos(\Theta) - 1) + 2\cos(\Theta)]. \quad (D19)$$

[65] The normalized scattering coefficients (D10) to (D14) can be interpreted as the pdf for the propagation angles (Θ, Φ) of the scattered particles in a local frame. The colatitude and longitude are measured from the incident propagation direction and the polarization direction, respectively. Note that for incident P wave, the definition of the angle Φ is arbitrary.

D3. Transformation of Angles

[66] Since the propagation and polarization directions of a scattered particle are selected in a local coordinate system, they must be rotated to the global coordinate system described in section A. The geometry of this transformation is depicted in Figure D1. Let the direction of the incident particle be given by the polar coordinates (θ_i, ϕ_i). The polarization of the incident particle is given by ψ_i which is the angle between the polarization axis and the vertical plane that contains the incident ray. The two angles that describe the scattering process are the scattering angle Θ and Φ, the angle between the scattering plane and the initial polarization direction. To express the polar angle θ_s and azimuth ϕ_s of the scattered particle in terms of the direction of the incoming particle (θ_i, ϕ_i) and the scattering and polarization angles (Θ, Φ, ψ_i), one can use spherical trigonometry. The polar angle of the scattered particle θ_s can be expressed as

$$\cos(\theta_s) = \cos(\theta_i)\cos(\Theta) + \sin(\theta_i)\sin(\Theta)\cos(\psi_i + \Phi). \quad (D20)$$

The azimuth ϕ_s of the scattered particle is given by

$$\cos(\phi_i - \phi_s) = \frac{\cos(\Theta) - \cos(\theta_i)\cos(\theta_s)}{\sin(\theta_i)\sin(\theta_s)}. \quad (D21)$$

To find the polarization angle of the scattered particle, the angle ψ_s between the scattering plane and the vertical plane that contains the scattered ray is calculated using

$$\sin(\psi_s) = \frac{\sin(\phi_i - \phi_s)}{\sin(\Theta)} \sin(\theta_i). \quad (D22)$$

The polarization direction of the scattered particle is either ψ_s as given by equation (D22) if the polarization is parallel to the scattering plane or $\psi_s + \pi/2$ if the polarization is perpendicular.

D4. Total Scattering Coefficients

[67] If a particle undergoes scattering, the probability distribution of the direction in which the particle continues to propagate is given by the scattering coefficients (D10) to
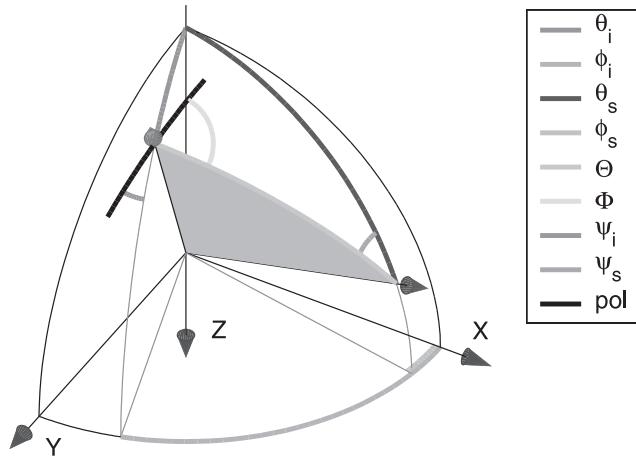
Figure D1. Illustration of the scattering and the polarization angle and their relation to the global polar coordinate system. Red and blue arrows indicates the directions of the incoming and scattered particle, respectively. The polarization direction of the incoming S particle is indicated by the bold black line.

(D14). The integral of the scattering coefficients over the solid angle gives the total scattering coefficient g_0^{AB}, from which we can define the probability that a certain scattering event from mode A to mode B occurs while the particle moves one unit length [*Sato and Fehler*, 1998, p. 43]:

$$g_0^{AB} \equiv \frac{1}{4\pi} \oint g^{AB} d\Omega = \frac{1}{l^{AB}}; \qquad (D23)$$

g_0^{SS} is the sum of the total scattering coefficients for the two different polarizations. The inverse of g_0^{AB} is the conversion mean free path l^{AB}, i.e, the average length that a particle of type A propagates until it is scattered into mode B. The length l^A defined as

$$l^A = \left(\sum_B g_0^{AB} \right)^{-1} \qquad (D24)$$

is the total mean free path of wave mode A. The free path length L^A of a particle of mode A between two scattering events is determined by the exponential probability distribution

$$\Pi(L^A) = (1/l^A) \exp(-L^A/l^A), \qquad (D25)$$

consistent with the scattering loss term in the equation of radiative transfer.

D5. Random Walk

[68] In sections D1–D4 we have outlined how the probability distributions for the scattering events are related to the properties of the medium. Here we combine these information and explain how it is used to simulate the random walk of the particles. This is largely analogous to *Margerin et al.* [2000]. The random walk is performed in incremental time steps Δt. Depending on their velocity the particles move paths of length Δl in this time. The probability of an incident particle of mode M_i to be scattered while moving Δl is according to equation (D25)

$$\Pi(M_i) = 1 - \exp\left(\frac{-\Delta l}{l^{M_i}} \right). \qquad (D26)$$

A first uniform random number $\epsilon_1 \in (0, 1)$ is used to decide whether a particle is scattered by comparing it to $\Pi(M_i)$. If $\epsilon_1 < \Pi(M_i)$ scattering occurs.

[69] In this case the mode of the outgoing particle M_o is selected according to the conditional probability distribution

$$\Pi(M_i|M_o) = \frac{g_0^{M_iM_o}}{\sum_{M_o} g_0^{M_iM_o}}. \qquad (D27)$$

It is the probability that a particle is scattered into mode M_o given that the incident mode is M_i. For the selection of the outgoing mode a second uniform random number $\epsilon_2 \in (0, 1)$ is used. Here the two S polarizations are considered different modes, which means that in the case of an incoming S particle it is decided at this point whether the outgoing particle is polarized parallel or perpendicular to the scattering plane, i.e., whether the new direction is selected using g_l^{SS} or g_r^{SS}. This choice also determines the polarization of the outgoing particle.

[70] Because of the special form of the scattering coefficients (equations (D10) to (D14)) that are used to select the new directions of the particle, and the assumption of linear polarization, the probability distributions of the scattering angle Θ and angle Φ are independent. The probability of the angle Θ under the condition that the incoming particle of mode M_i is scattered into mode M_o is

$$\Pi(M_i, M_o|\Theta) = \frac{\int g^{M_iM_o}(\Theta, \Phi) d\Phi}{4\pi g_0^{M_iM_o}}. \qquad (D28)$$

The probability of the angle Φ is

$$\Pi(M_i, M_o|\Phi) = \frac{\int g^{M_iM_o}(\Theta, \Phi) \sin(\Theta) d\Theta}{4\pi g_0^{M_iM_o}}. \qquad (D29)$$

For fast evaluation of the probability distributions $\Pi(M_i, M_o|\Theta)$ and $\Pi(M_i, M_o|\Phi)$ during the simulation we generate lists of numbers drawn from these distributions prior to the simulation (Appendix H). This means that lists with values of Θ are generated for the five types of scattering that can occur, namely $P \to P$, $P \to S$, $S \to P$, $S \to S_l$, and $S \to S_r$. For the angle Φ only a single list has to be generated with numbers distributed according to $\sin^2(\Phi)$. Numbers with a $\cos^2(\Phi)$ distribution are obtained by adding $\pi/2$ to the $\sin^2(\Phi)$ distributed numbers. In the cases of $P \to P$ and $P \to S$ scattering the values for the angle Φ are uniformly distributed in $[0, 2\pi]$. Two additional uniformly distributed random numbers ϵ_3 and ϵ_4 are used to select values for

Θ and Φ from the appropriate list of numbers with the needed probability distribution.

[71] Since the radiative transfer equations in section 2.2 are written as a three-mode system, the I_θ^S and I_ϕ^S intensities could be computed independently. However, for the modeling of Lg coda waves, only the sum of I_θ^S and I_ϕ^S is relevant, which reduces the need of averaging. It implies that the angle Φ (equation (D29)) is measured from the direction of polarization of an incoming S particle (compare Figure D1).

[72] The separate treatment of parallel and perpendicular $S \rightarrow S$ scattering is particularly convenient since the probabilities of Θ and Φ turn out to be independent. This greatly simplifies the simulation but may seem unphysical because the outgoing particle has to be polarized either parallel or perpendicular to the scattering plane. However, we note that the correct polarization of the $S \rightarrow S$ scattering is obtained after averaging over a number of particles. More general results concerning elliptical polarizations are presented by *Chandrasekhar* [1960].

Appendix E: Intrinsic Attenuation

[73] If the intrinsic attenuation is uniform in space and equal for all modes it can be accounted for by the multiplication of the envelopes with an exponentially decaying function after the simulation. In the elastic case where two different wave modes with different attenuation properties are modeled, the attenuation has to be taken into account during the simulation. There are two possibilities for this. The particles can either have constant energy but die off after a certain time with a probability depending on the attenuation or the energy of the particles is decreased continuously as they propagate.

[74] The parameter that is usually used to describe the amount of intrinsic attenuation is the intrinsic quality factor ^IQ or its reciprocal quantity the attenuation parameter $^IQ^{-1}$. The attenuation parameter is proportional to the exponential decay rate of seismic wave amplitude with distance. In a nonscattering medium the energy density of a plane wave decays like

$$E^P(r,f) \propto e^{\frac{-\omega r}{\alpha_0^I Q^P}} \quad \text{and} \quad E^S(r,f) \propto e^{\frac{-\omega r}{\beta_0^I Q^S}}. \tag{E1}$$

Here ω denotes angular frequency and superscripts P and S indicate the respective modes with their mean wave velocities α_0 and β_0. In equation (13) this decay is only described correctly for infinitesimal Δl. For finite size path length Δl the probability that a particle dies off can be calculated from (E1) to be

$$\Pi^P(\Delta l) = 1 - e^{\frac{-\omega \Delta l}{\alpha_0^I Q^P}} \quad \text{and} \quad \Pi^S(\Delta l) = 1 - e^{\frac{-\omega \Delta l}{\beta_0^I Q^S}} \tag{E2}$$

for P and S waves, respectively. These are also the factors that the Stokes vector has to be multiplied with to account for the loss of energy if the particles keep propagating. The latter strategy has been adopted in the present algorithm because it accelerates the convergence of the energy density estimates in the later part of the envelopes.

Appendix F: Ray Tracing

[75] Once the mode and direction of a particle are fixed, it propagates through the medium according to ray theory [e.g., *Aki and Richards*, 1980]. This includes the interaction with interfaces, where particles can be reflected or transmitted just like seismic waves. They can also change polarization if conversion occurs. The particles move along straight lines or curved rays depending on the complexity of the background medium. The algorithm is capable of dealing with any depth-dependent velocity structure but neglects any diffraction effect associated with caustics, for instance.

F1. Interfaces

[76] If a particle hits an interface between two media characterized by different mass densities and wave velocities it can be reflected, transmitted or converted. The probabilities for the particle to undergo either of these events are given by the respective energy reflection coefficients. These will be expressed in the notation of *Aki and Richards* [1980]. Assuming horizontal interfaces, acute and grave accents are used to indicate upgoing and downgoing particles, respectively. The general form of an energy reflection coefficient is

$$\Pi(\tilde{A} \rightarrow \hat{B}) = \frac{\rho_o v_o \cos(\gamma_o)}{\rho_i v_i \cos(\gamma_i)} (\tilde{A}\hat{B})^2. \tag{F1}$$

Here $\Pi(\tilde{A} \rightarrow \hat{B})$ is the energy reflection coefficient, i.e., the probability that an incoming particle of type A with direction $\tilde{}$ continues in direction $\hat{}$ as type B. $\tilde{A}\hat{B}$ is the reflection coefficient for displacement amplitudes. A and B stand for the wave types P or S and $\tilde{}$ and $\hat{}$ stand for the accents $\acute{}$ or $\grave{}$ indicating upgoing or downgoing directions. For an interface between two solids, all 16 combinations of P, S, $\acute{}$ and $\grave{}$ are defined. ρ and v indicate mass density and wave velocity, respectively; γ is the angle between the direction of the ray and the normal to the interface. Subscripts i and o indicate the medium on the side of the incoming or outgoing particle, respectively. The velocity, however, does not only depend on the medium but also on the wave type.

[77] For horizontal interfaces the two different S wave polarizations can be treated separately. For horizontally polarized waves there is no conversion into other modes. The reflection coefficients for displacement amplitudes for this case are given by *Aki and Richards* [1980, equation 5.33, p. 139]. For vertically polarized S waves and P waves which are coupled at the interface the amplitude reflection coefficients are given by *Aki and Richards* [1980, equations 5.40, pp. 144–145]. Interaction with the free surface causes total reflection for horizontally polarized S waves. The displacement amplitude coefficients for vertically polarized S and P waves are given by *Aki and Richards* [1980, equations 5.27, 5.28 (p. 134), 5.31, and 5.32 (p. 136)]. Any supercritical reflection of S energy is treated like total

reflection and neglects the phase shifts between the two S polarizations, thereby neglecting elliptical polarization.

F2. Raypaths in a Medium With Vertical Velocity Variations

[78] Ray theory predicts that in a laterally homogeneous medium the particles propagate on curved rays in a vertical plane. In spherical coordinates the azimuthal angle ϕ of the velocity vector remains constant and only the polar angle varies along the path. The curvature of the ray is determined by the velocity gradient. In order to use the usual notation of Snell's law we introduce the incidence angle $\alpha = \pi - \theta$ for θ as defined in Figure 2. In this notation, Snell's law states that

$$\frac{\sin(\alpha)}{v} = q = \text{const.} \tag{F2}$$

Here v is the wave velocity of either P or S waves and the constant q is called the ray parameter. In order to keep q constant along a ray that passes through regions with changing velocity the relative change of $\sin(\alpha)$ must balance the relative change of v. Differentiation equation (F2), one obtains

$$\frac{d\alpha}{ds} = \frac{dv}{dz}\frac{\sin(\alpha)}{v}, \tag{F3}$$

where the last factor can be recognized as the ray parameter. Equation (F3) determines the change of incidence angle along the ray. For a constant velocity gradient dv/dz the raypath is a circle. With equation (F3) we can approximately model the particle propagation in any depth-dependent velocity structure by simply changing the θ component of the velocity vector after the propagation of a path element Δl by an amount of $-(\sin(\theta)dv/vdz)\Delta l$.

Appendix G: Recording of Particles

[79] For each random walk, the energy of the particle is stored in a four-dimensional array which represents rectangular boxes in three-dimensional space with a fourth dimension for time. Like in a histogram, the contribution of each particle is recorded by adding its energy to the cell of the array in which the particle resides. Snapshots of the energy field are taken in time intervals Δt. This way we obtain a spatiotemporal estimate of the local energy density as defined by equation (1) for directions integrated over the whole solid angle. In the simulation of the situation in the Pyrenees in sections 5 and 6 we use cells of 4 km side length and $\Delta t = 1$ s.

Appendix H: Evaluation of Probability Distributions

[80] A key point in Monte Carlo simulations is the evaluation of probability distributions. In the present algorithm the most critical part is the generation of random numbers for the scattering angles. Since, during a simulation a large quantity of random numbers with various probability distributions is needed, it is useful for the computational efficiency to generate lists of such numbers prior to the simulation. We use an iterative trial and reject method to generate random numbers with arbitrary probability distributions. This method does a random sampling of a given probability distribution $P(x)$. A set X of N random numbers $x_i \in [x_{\min}, x_{\max}]$, $i = 1, \ldots, N$ having the distribution $P(x)$ is selected as a subset of a uniformly distributed set Y of random numbers $y_j \in [y_{\min}, y_{\max}]$, $j = 1, \ldots, M$. The random number y_j belongs to X if $z_j \leq P(y_j)/P_{\max}$ with $z_j \in [0, 1]$ being another random number from a uniformly distributed set. $P(x)/P_{\max}$ is the normalized probability distribution where $P_{\max}$ is the maximum of $P(x)$. As an approximate estimate of $P_{\max}$ we use $P_{\max} = \max_{j=1,\ldots,M}(P(y_j))$. This method is similar to the Metropolis-Hastings algorithm [*Hastings*, 1970] with uniform proposal density. The probability distributions encountered here depend on two angular variables. But as can be seen in equations (D10)–(D14) the two variables are independent and the joint two-dimensional probability distribution is the product of the two one-dimensional distributions. However, the trial and reject method as explained above can be generalized to multi-dimensional probability distributions.

References

Aki, K., and B. Chouet (1975), Origin of coda waves: Source, attenuation, and scattering effects, *J. Geophys. Res.*, *80*, 3322–3342, doi:10.1029/JB080i023p03322.

Aki, K., and P. G. Richards (1980), *Quantitative Seismology, Theory and Methods*, vol. I, W. H. Freeman, San Francisco, Calif.

Apresyan, L., and Y. A. Kravtsov (1996), *Radiation Transfer: Statistical and Wave Aspects*, Gordon and Breach, Amsterdam.

Baumgardt, D. R. (2001), Sedimentary basins and the blockage of Lg wave propagation in the continents, *Pure Appl. Geophys.*, *158*, 1207–1250, doi:10.1007/PL00001221.

Birch, F. (1961), The velocity of compressional waves in rocks to 10 kilobars, part 2, *J. Geophys. Res.*, *66*, 2199–2224, doi:10.1029/JZ066i007p02199.

Bormann, P. (Ed.) (2002), *New Manual of Seismological Observatory Practice*, Dtsch. GeoForschungsZentrum, IASPEI, Potsdam, Germany.

Campillo, M., B. Feigner, M. Bouchon, and N. Bethoux (1993), Attenuation of crustal waves across the Alpine range, *J. Geophys. Res.*, *98*, 1987–1996, doi:10.1029/92JB02357.

Chandrasekhar, S. (1960), *Radiative Transfer*, Dover, New York.

Chazalon, A., M. Campillo, R. Gibson, and E. Carreno (1993), Crustal wave propagation anomaly across the Pyrenean Range: Comparison between observations and numerical simulations, *Geophys. J. Int.*, *115*, 829–838, doi:10.1111/j.1365-246X.1993.tb01495.x.

Choukroune, P. (1992), Tectonic evolution of the Pyrenees, *Annu. Rev. Earth Planet. Sci.*, *20*, 143–158, doi:10.1146/annurev.ea.20.050192.001043.

Daigniéres, M., J. Gallart, and E. Banda (1981), Lateral variation of the crust in the North Pyrenean zone, *Ann. Geophys.*, *37*, 435–456.

Dainty, A. M., and M. N. Toksöz (1981), Seismic codas on the Earth and the Moon: A comparison, *Phys. Earth Planet. Inter.*, *26*, 250–260, doi:10.1016/0031-9201(81)90029-7.

Dziewonski, A. M., and D. L. Anderson (1981), Preliminary reference Earth model, *Phys. Earth Planet. Inter.*, *25*, 297–356, doi:10.1016/0031-9201(81)90046-7.

Fehler, M., M. Hoshiba, H. Sato, and K. Obara (1992), Separation of scattering and intrinsic attenuation for the Kanto-Tokai region, Japan, using measurements of S-wave energy versus hypocentral distance, *Geophys. J. Int.*, *108*(3), 787–800.

Gusev, A. A., and I. R. Abubakirov (1987), Monte-Carlo simulation of record envelope of a near earthquake, *Phys. Earth Planet. Inter.*, *49*, 30–36, doi:10.1016/0031-9201(87)90130-0.

Gusev, A. A., and I. R. Abubakirov (1996), Simulated envelopes of non-isotropically scattered body waves as compared to observed ones: Another manifestation of fractal heterogeneity, *Geophys. J. Int.*, *127*(1), 49–60, doi:10.1111/j.1365-246X.1996.tb01534.x.

Hastings, W. K. (1970), Monte Carlo sampling methods using Markov chains and their applications, *Biometrika*, *57*, 97–109, doi:10.1093/biomet/57.1.97.

Hennino, R., N. Trégourès, N. M. Shapiro, L. Margerin, M. Campillo, B. van Tiggelen, and R. L. Weaver (2001), Observation of equipartition of seismic waves, *Phys. Rev. Lett.*, *86*, 3447–3450, doi:10.1103/PhysRevLett.86.3447.

Hoshiba, M. (1991), Simulation of multiple-scattered coda wave excitation based on the energy conservation law, *Phys. Earth Planet. Inter.*, *67*, 123–136.

Hoshiba, M. (1993), Separation of scattering attenuation and intrinsic absorption in Japan using the multiple lapse time window analysis of full seismogram envelope, *J. Geophys. Res.*, *98*, 15,809–15,824.

Hoshiba, M. (1995), Estimation of nonisotropic scattering in western Japan using coda wave envelopes: Application of a multiple nonisotropic scattering model, *J. Geophys. Res.*, *100*, 645–657.

Hoshiba, M. (1997), Seismic coda wave envelope in depth-dependent S wave velocity structure, *Phys. Earth Planet. Inter.*, *104*, 15–22.

Hoshiba, M., H. Sato, and M. Fehler (1991), Numerical basis of the separation of scattring and intrinsic absorption from full seismogram envelope - A Monte-Carlo simulation of multiple isotropic scattering, *Pap. Meteorol. Geophys.*, *42*, 265–291.

Ishimaru, A. (1978), *Wave Propagation and Scattering in Random Media*, vol. 1 and 2, Academic, New York.

Lacombe, C., M. Campillo, A. Paul, and L. Margerin (2003), Separation of intrinsic absorption and scattering attenuation from Lg coda decay in central France using acoustic radiative transfer theory, *Geophys. J. Int.*, *154*(2), 417–425.

Larose, E., L. Margerin, B. A. van Tiggelen, and M. Campillo (2004), Weak localization of seismic waves, *Phys. Rev. Lett.*, *93*(4), 048501, doi:10.1103/PhysRevLett.93.048501.

Lux, I., and L. Kolbinger (1991), *Monte Carlo Particle Transport Methods: Neutron and Photon Calculations*, CRC Press, Boca Raton, Fla.

Margerin, L. (2005), Introduction to radiative transfer of seismic waves, in *Seismic Data Analysis With Global and Local Arrays, Geophys. Monogr. Ser.*, vol. 157, edited by A. Levander and G. Nolet, pp. 229–252, AGU, Washington, D. C.

Margerin, L., M. Campillo, and B. A. Van Tiggelen (1998), Radiative transfer and diffusion of waves in a layered medium: New insight into coda Q, *Geophys. J. Int.*, *134*, 596–612.

Margerin, L., M. Campillo, and B. Van Tiggelen (2000), Monte Carlo simulation of multiple scattering of elastic waves, *J. Geophys. Res.*, *105*, 7873–7892, doi:10.1029/1999JB900359.

McNamara, D. E., and W. R. Walter (2001), Mapping crustal heterogeneity using Lg propagation efficiency throughout the Middle East, Mediterranean, southern Europe and northern Africa, *Pure Appl. Geophys.*, *158*, 1165–1188.

Mitchell, M. (1996), *An Introduction to Genetic Algorithms*, MIT Press, Cambridge, Mass.

Pous, J., J. Ledo, A. Marcuello, and M. Daignières (1995), Electrical resistivity model of the crust and upper mantle from manetotelluric survey through the central Pyrenees, *Geophys. J. Int.*, *121*, 750–762.

Przybilla, J., M. Korn, and U. Wegler (2006), Radiative transfer of elastic waves versus finite difference simulations in two-dimensional random media, *J. Geophys. Res.*, *111*, B04305, doi:10.1029/2005JB003952.

Rodgers, A. J., J. F. Ni, and T. M. Hearn (1997), Propagation characteristics of short-period Sn and Lg in the Middle East, *Bull. Seismol. Soc. Am.*, *87*(2), 396–413.

Ryzhik, L., G. Papanicolaou, and J. B. Keller (1996), Transport equations for elastic and other waves in random media, *Wave Motion*, *24*, 327–370.

Sato, H., and M. C. Fehler (1998), *Seismic Wave Propagation and Scattering in the Heterogeneous Earth*, Springer, New York.

Sens-Schönfelder, C., and U. Wegler (2006), Radiative transfer theory for estimation of the seismic moment, *Geophys. J. Int.*, *167*(3), 1363–1372, doi: 10.1111/j.1365-246X.2006.03139.x.

Shapiro, N., N. Béthoux, M. Campillo, and A. Paul (1996), Regional seismic phases across the Ligurian Sea: Lg blockage and oceanic propagation, *Phys. Earth Planet. Inter.*, *93*, 257–268.

Shearer, P. M. (1999), *Introduction to Seismology*, Cambridge Univ. Press, Cambridge, U. K.

Shearer, P. M., and P. S. Earle (2004), The global short-period wavefield modelled with a Monte Carlo seismic phonon method, *Geophys. J. Int.*, *158*, 1103–1117, doi:10.1111/j.1365-246X.2004.02378.x.

Shearer, P. M., and P. S. Earle (2008), Observing and modeling elastic scattering in the deep Earth, in *Earth Heterogeneity and Scattering Effects on Seismic Waves, Adv. Geophys.*, vol. 50, edited by H. Sato and M. C. Fehler, pp. 167–193, Elsevier Ltd., Oxford.

Souriau, A., and M. Granet (1995), A tomographic study of the lithosphere beneath the Pyrenees from local and teleseismic data, *J. Geophys. Res.*, *100*, 18,117–18,134, doi:10.1029/95JB01053.

Souriau, A., M. Sylvander, A. Rigo, J. Fels, J. Douchain, and C. Ponsolles (2001), Sismotectonique des Pyrénées: Principales contraintes sismologiques, *Bull. Soc. Geol. Fr.*, *172*(1), 25–39.

Turner, J. A. (1998), Scattering and diffusion of seismic waves, *Bull. Seismol. Soc. Am.*, *88*(1), 276–283.

Turner, J. A., and R. L. Weaver (1994), Radiative transfer and multiple scattering of diffuse ultrasound in polycrystalline media, *Acoust. Soc. Am. J.*, *96*, 3675–3683.

Vacher, P., and A. Souriau (2001), A three-dimensional model of the Pyrenean deep structure based on gravity modelling, seismic images and petrological constraints, *Geophys. J. Int.*, *145*, 460–470, doi:10.1046/j.0956-540X.2001.01393.x.

Weaver, R. L. (1990), Diffusivity of ultrasound in polycrystals, *J. Mech. Phys. Solids*, *38*, 55–86.

Wegler, U., and B. G. Lühr (2001), Scattering behaviour at Merapi volcano (Java) revealed from an active seismic experiment, *Geophys. J. Int.*, *145*(3), 579–592, doi:10.1046/j.1365-246x.2001.01390.x.

Yoshimoto, K. (2000), Monte Carlo simulation of seismogram envelopes in scattering media, *J. Geophys. Res.*, *105*, 6153–6162, doi:10.1029/1999JB900437.

_____

M. Campillo, Laboratoire de Géophysique Interne et Tectonophysique, Université Joseph Fourier, B.P. 53, F-38041 Grenoble CEDEX 9, France. (campillo@obs.ujf-grenoble.fr)

L. Margerin, Centre Européen de Recherche et d'Enseignement des Géosciences de l'Environnement, Europôle Méditerranéen de l'Arbois, B.P. 80, F-13545 Aix en Provence CEDEX 04, France. (margerin@cerege.fr)

C. Sens-Schönfelder, Institute of Geophysics and Geology, Department of Physics and Geosciences, University of Leipzig, Talstrasse 35, D-04103 Leipzig, Germany. (sens-schoenfelder@uni-leipzig.de)